To appear in The Astrophyical Journal

The ACS Survey of Galactic Globular Clusters. IX.[1] Horizontal Branch Morphology and the Second Parameter Phenomenon

Aaron Dotter

Department of Physics and Astronomy, University of Victoria, PO Box 3055, STN CSC, Victoria, BC, V8W 3P6 Canada

dotter@uvic.ca

Ata Sarajedini

Department of Astronomy, University of Florida, 211 Bryant Space Science Center, Gainesville, FL 32611

ata@astro.ufl.edu

Jay Anderson

Space Telescope Science Institute, 3700 San Martin Drive, Baltimore, MD 21218, USA

Antonio Aparicio

Instituto de Astrofísica de Canarias, Vía Láctea s/n, E-38200 La Laguna, Spain

Luigi R. Bedin

Space Telescope Science Institute, 3700 San Martin Drive, Baltimore, MD 21218, USA

Brian Chaboyer

Department of Physics and Astronomy, Dartmouth College, 6127 Wilder Laboratory, Hanover, NH 03755

Steven Majewski

Dept. of Astronomy, University of Virginia, P.O. Box 400325, Charlottesville, VA 22904-4325

A. Marín-Franch

Instituto de Astrofísica de Canarias, Vía Láctea s/n, E-38200 La Laguna, Spain

Antonino Milone

Dipartimento di Astronomia, Università di Padova, 35122 Padova, Italy

Nathaniel Paust

Space Telescope Science Institute, 3700 San Martin Drive, Baltimore MD 21218

Giampaolo Piotto

Dipartimento di Astronomia, Università di Padova, 35122 Padova, Italy

I. Neill Reid

Space Telescope Science Institute, 3700 San Martin Drive, Baltimore MD 21218

Alfred Rosenberg

Instituto de Astrofísica de Canarias, Vía Láctea s/n, E-38200 La Laguna, Spain

Michael Siegel

Department of Astronomy and Astrophysics, Pennsylvania State University, 525 Davey Laboratory, State College, PA 16801

ABSTRACT

The horizontal branch (HB) morphology of globular clusters (GCs) is most strongly influenced by metallicity. The second parameter phenomenon, first described in the 1960's, acknowledges that metallicity alone is not enough to describe the HB morphology of all GCs. In particular, astronomers noticed that the outer Galactic halo contains GCs with redder HBs at a given metallicity than are found inside the Solar circle. Thus, at least a second parameter was required to characterize HB morphology. While the term 'second parameter' has since come to be used in a broader context, its identity with respect to the original problem has not been conclusively determined. Here we analyze the median color difference between the HB and the red giant branch (RGB), hereafter denoted $\Delta(V-I)$, measured from Hubble Space Telescope (HST) Advanced Camera for Surveys (ACS) photometry of 60 GCs within $\sim$20 kpc of the Galactic Center.

Analysis of this homogeneous data set reveals that, after the influence of metallicity has been removed from the data, the correlation between $\Delta(V-I)$ and age is stronger than that of any other parameter considered. Expanding the sample to include HST ACS and Wide Field Planetary Camera 2 (WFPC2) photometry of the 6 most distant Galactic GCs lends additional support to the correlation between $\Delta(V-I)$ and age. This result is robust with respect to the adopted metallicity scale and the method of age determination, but must bear the caveat that high quality, detailed abundance information is not available for a significant fraction of the sample. Furthermore, when a subset of GCs with similar metallicities and ages are considered, a correlation between $\Delta(V-I)$ and central luminosity density is exposed. With respect to the existence of GCs with anomalously red HBs at a given metallicity, we conclude that age is the second parameter and central density is most likely the third. Important problems related to HB morphology in GCs, notably multi-modal distributions and faint blue tails, remain to be explained.

Subject headings: globular clusters: general

1. Introduction

It has been clear for decades that metallicity is the most influential factor governing the HB morphologies of Galactic GCs: metallicity is the first parameter. The earliest photographic color-magnitude diagrams (CMDs) of GCs by, e.g. Arp et al. (1952); Sandage (1953), revealed that HB stars in metal-rich GCs tend to lie on the red side of the RR Lyrae instability strip while HB stars in metal-poor GCs lie primarily on the blue side. As more and more CMDs were assembled, exceptions to this rule were uncovered. Sandage & Wallerstein (1960) noted that M 13 and M 22 display HB morphologies appropriate for metal-poor GCs, despite the fact both GCs were of intermediate metallicity, and suggested that a difference in age might be responsible. Sandage & Wildey (1967) noticed that the HB of NGC 7006 is redder than either M 13 or M 3, despite the fact that all three GCs appeared to have very similar metallicities. Such anomalies suggested the need for a second parameter that could account for differences in HB morphology not obviously caused by metallicity. van den Bergh

[1]Based on observations with the NASA/ESA *Hubble Space Telescope*, obtained at the Space Telescope Science Institute, which is operated by AURA, Inc., under NASA contract NAS 5-26555, under program GO-10775.

(1965) summarized the problem, stating that metallicity is not sufficient to explain the extent of observed HB morphologies but that differences in age or He enrichment could explain the observed variations. Both of these suggestions remain valid up to the present time. van den Bergh (1967) analyzed the integrated colors of 49 GCs with UBV photometry and concluded that 'at least two parameters (one of which is metal abundance) are required to describe globular clusters.'

The second parameter phenomenon took on a greater significance with the seminal work of Searle & Zinn (1978). Searle & Zinn recognized that GCs with unusually red HBs are relatively rare in the inner regions of the Galactic halo (Galactocentric radius, $R_{GC} \lesssim 8$ kpc) but become increasingly common at greater R_{GC} (see their Figure 10). Searle & Zinn used this fact to argue that the inner halo was assembled early and in a fairly short time while the outer halo was assembled over an extended period of time. Current galaxy formation scenarios envision the outer regions of the Galaxy as the accumulated debris of the many accretion events that shaped the early evolution of the Galaxy. In that context, understanding the origin and existence of age and metallicity gradients in the Galactic GC population is as relevant now as it was at the time when Searle & Zinn first introduced their halo formation scenario.

Subsequent efforts relating to the second parameter problem fall into two general categories: those that attempt to measure the age difference between two (or a few) GCs with similar metallicities but markedly different HB morphologies and those that investigate the ensemble properties of a large sample of GCs.

One canonical pair in the former category is NGC 288, with a blue HB, and NGC 362, with a red HB. The first CCD-based, differential photometric study of these clusters was conducted by Bolte (1989). Bolte concluded that NGC 288 is ∼3 Gyr older than NGC 362. The subsequent work of Green & Norris (1990), Sarajedini & Demarque (1990), and VandenBerg et al. (1990) echoed this result. By contrast, VandenBerg & Durrell (1990) reached a very different conclusion. Using the brightest RGB star in each GC, VandenBerg & Durrell (1990) corrected the photometry of NGC 288 and NGC 362 for their relative distances and found their main sequence turnoffs to be roughly coincident, thereby suggesting a negligible age difference. Bellazzini et al. (2001) found NGC 288 to be 2±1 Gyr older than NGC 362 using three different techniques; in a follow-up, Catelan et al. (2001a) found that an age difference of 2 Gyr was plausible if both GCs have [Fe/H] ~ -1.2 but that their synthetic HB models were unable to match the detailed HB morphology of either GC using canonical assumptions of average mass loss and dispersion on the HB. In considering differences between second parameter pairs, it is important to understand just how similar the abundances are in both clusters. Shetrone & Keane (2000) performed a detailed comparison of abundances in red

giants with 13 stars in NGC 288 and 12 in NGC 362. These authors concluded that NGC 288 has a lower [Fe/H] than NGC 362 by 0.06 dex, that the average [α/Fe] ratios are very similar, and that both GCs exhibit variations among O, Na, and Al.

The other canonical second parameter pair is M 13, with a blue HB, and M 3, with an intermediate HB. M 13 and M 3 are ∼0.2 dex more metal poor than NGC 288 and NGC 362. VandenBerg et al. (1990) found evidence for an age difference but the quality of their CMDs did not allow a more definitive statement. Catelan & de Freitas Pacheco (1995) estimated an upper limit to the age difference of ∼3 Gyr and concluded that it was insufficient to explain the HB morphologies, assuming both GCs have the same chemical composition. Alternatively, Johnson & Bolte (1998) suggested the difference in their HB morphologies was due to a difference in their He abundances. Johnson & Bolte suggested that M 13 had a He mass fraction ∼0.05 greater than M 3. However, Sweigart & Catelan (1998) showed that a difference of $\Delta Y \sim 0.05$ at constant [Fe/H] would make the level of the HB brighter by ∼0.2 mag. Such a difference between M 3 and M 13 was ruled out by the photometry of Rey et al. (2001), who also concluded that M 13 is older than M 3 by 1.7 ± 0.7 Gyr. Sneden et al. (2004) compared spectra of 28 red giants in M 3 with 35 in M 13 and found the two GCs' mean [Fe/H] values the same within their 1-σ error bars. However, Sneden et al. (2004) reported differences in light element abundance variations, particularly O, for which M 13 displays a larger range of variation than M 3 by ∼0.5 dex.

A discussion of the search for the second parameter in GC-to-GC comparisons would not be complete without including the work of Stetson et al. (1999) and Dotter et al. (2008b). These investigations used HST WFPC2 photometry to measure the ages of the outer halo GCs Palomar 3, Palomar 4, and Eridanus (Stetson et al. 1999) and AM-1 and Palomar 14 (Dotter et al. 2008b) relative to inner halo GCs with similar metallicities, M3 and M5[2]. Each of the five outer halo GCs has a redder HB morphology than its comparison inner halo GC. Both studies concluded that the outer halo GCs are ∼1.5-2 Gyr younger than M3 and M5, provided the chemical compositions of the outer halo GCs are comparable to their inner halo counterparts. A recent study by Koch et al. (2009) found the abundances of Pal 3 are essentially the same as inner halo GCs of similar metallicity and thus the relative age comparison with M 3 by Stetson et al. (1999) was justified. Overall, the outer halo GCs' chemical compositions remain poorly understood by comparison with the inner halo, see e.g. Pritzl et al. (2005). Catelan (2000) found the reported age differences between Pal 4 and Eridanus, with red HBs, and M 5, with an intermediate HB, too small to explain the difference in HB morphologies unless all three GCs are younger than 10 Gyr, assuming

[2]There is substantial evidence that M 5 is actually an outer halo GC currently near its perigalacticon, see Scholz et al. (1996) and Dinescu et al. (1999).

standard assumptions of mass loss on the RGB. Catelan et al. (2001b) concluded that it was possible to explain the difference in HB morphology between Pal 3 and M 3 if the former has less HB mass dispersion and is younger than the latter. These examples indicate that if age is the second parameter, then it is our lack of understanding of mass loss that confuses GC-to-GC comparisons as first pointed out by Rood (1973). The review by Catelan (2009) includes a thorough discussion of different mass loss prescriptions and their efficacy. Given the HB morphologies and relatively young ages of the most distant outer halo GCs[3], it is important to include them when considering the properties of the entire Galactic GC population, especially in the context of Searle & Zinn's halo formation scenario.

The second category of second parameter studies are those that consider the properties of a large sample of Galactic GCs, e.g. Searle & Zinn (1978). In the first CCD-era study, Sarajedini & King (1989) compiled properties for 31 Galactic GCs. Among other things, Sarajedini & King (1989) examined the variation of HB morphology with age for GCs in a narrow range of metal abundance and showed that GCs with red HBs are significantly younger than those with blue HBs by as much as 5 Gyr. The subsequent studies of Chaboyer et al. (1992), Sarajedini et al. (1995), and Chaboyer et al. (1996) updated and reaffirmed this result. Rosenberg et al. (1999) found that the GCs with $R_{GC} > 8$ kpc are, on average, younger than those with $R_{GC} < 8$ kpc, which is consistent with age as the second parameter. By contrast, Richer et al. (1996) examined the CMDs of 36 GCs, found an age dispersion of $\sim$1 Gyr with no significant age gradient in the Galactic halo, and concluded that this age range was too small for metallicity and age alone to explain HB morphology in GCs.

Theoretical efforts have provided further insights into the complexities of HB morphology. In particular, several studies have applied the synthetic HB model developed by Rood (1973). Lee et al. (1990), Catelan & de Freitas Pacheco (1993), and Lee et al. (1994) used synthetic HB models to explore the interplay of HB morphology, metallicity, and age in the CMD. These studies demonstrated considerable degeneracy in the HB morphology–metallicity diagram and, in particular, Catelan & de Freitas Pacheco (1993) argued that unless absolute values of the He abundance, [α/Fe] ratios, and RGB mass loss were known, HB morphology did not constitute a reliable age constraint. Nevertheless, Lee et al. (1994) concluded that there was evidence for an age dispersion of $\lesssim 5$ Gyr among Galactic GCs of similar metallicity but markedly different HB morphologies. A number of theoretical studies have also focused on second parameter pairs or triads but, unfortunately, the lack of a firm

[3]The exception in the outer halo is NGC 2419. A number of dedicated HST photometric studies have focused on this massive, distant GC. Harris et al. (1997) and Sandquist & Hess (2008) both found NGC 2419 to be an old, metal poor GC with a blue HB.

theoretical understanding of mass loss along the RGB has impaired the these efforts, as first pointed out by Rood (1973). See Catelan (2009) for a recent review.

As it pertains to HB morphology, the use of the term 'second parameter' has expanded to cover a broad range of complex behaviors. In particular, this includes the faint extent of the blue HB tail in some GCs. Fusi Pecci et al. (1993) analyzed 53 GCs and found that the length of the HB in the CMD–and the extent of the blue tail–is correlated with central density. Buonanno et al. (1997) also reported a link between an extended blue tail and central density in GCs and concluded that 'environment is "a" second parameter'. Smith (2004) showed that there is a correlation between central density and HB morphology for intermediate metallicity GCs ($-1.7 < [\mathrm{Fe/H}] < -1.3$) where the second parameter effect is most pronounced. Recio-Blanco et al. (2006) analyzed the properties of 54 Galactic GCs with homogeneous photometry from an HST WFPC2 Snapshot Survey (Piotto et al. 2002) and concluded that more massive GCs tend to have more extended blue HBs. Recio-Blanco et al. (2006) recognized a link between the effective temperature of the hottest HB star in a GC and its mass (as inferred from its integrated luminosity) and suggested that self-pollution could explain the existence of faint blue tails in preferentially massive GCs.

Evidence abounds for the presence of chemical abundance variations in all GCs (Gratton et al. 2004b; Carretta et al. 2009a,b) and the possible correlation between the degree of abundance variations and the faint extent of the blue HB (Carretta et al. 2007). However, it is unlikely that the existence of faint, blue tails in the HBs of some GCs is directly related to the appearance of anomalously red HBs in others. It is also unlikely that chemical abundance variations will unduly affect age estimates of most GCs, provided the total metal content is constant across all stars (Pietrinferni et al. 2009). For cases in which the total metal abundance is not constant, or there are distinct stellar populations present in the CMD, age estimates are necessarily more complicated and careful analysis of each of these GCs is needed. See Piotto (2009) for a recent summary of GCs with multiple stellar populations visible in the CMD, several of which were discovered with photometry from the ACS Survey of Galactic GCs. The complex issue of multiple stellar populations in GCs remains poorly understood and the extent to which multiple-population GCs permeate the Galactic GC population is unknown at present.

To summarize, the presence of metal poor GCs with red HBs that primarily reside in the outer Galactic halo is well-known observationally. Although the present study is focused on the Galactic GCs, including some of those associated with the Sagittarius dwarf, there is ample evidence to suggest that metal poor GCs with red HBs are also found in the Magellanic Clouds (Johnson et al. 1999; Glatt et al. 2008) and Fornax (Buonanno et al. 1999). Mackey & Gilmore (2004) summarize our current knowledge of the GC populations in the

Galaxy and its satellites in the HB morphology–metallicity diagram. Despite an abundance of observational evidence, no consensus has been reached as to what parameter(s) are responsible for the appearance of relatively red HBs in metal poor GCs. Age is frequently offered as a candidate but considerable doubt still remains because the age difference claimed–or required by theoretical studies of HB morphology–is too large to satisfy the observations.

The existence of a homogeneous database of deep, high quality photometry from the ACS Survey of Galactic GCs (Sarajedini et al. 2007, Paper I in this series) has motivated a re-examination of HB morphology and its relation to a variety of GC properties. The paper is organized as follows: §2 describes the data sample; §3 describes the methods that were employed to determine the HB morphologies; §4 describes the sources of GC ages and provides some discussion of complicating factors in age determination; §5 presents the analysis performed on the assembled data and discusses the important results; and, finally, §6 provides a summary of the salient points.

2. The observational data

2.1. The ACS Survey of Galactic GCs

The photometric catalog of the ACS Survey of Galactic GCs (Anderson et al. 2008, Paper V) consists of 65 GCs observed in $F606W$ and $F814W$. Most details concerning the data reduction and calibration are provided in Paper V but, since its publication, the data have been adjusted to account for updated HST/ACS Wide Field Channel zero-points (Bohlin 2007); the new $F606W$ and $F814W$ zeropoints are, respectively, 22 and 35 mmag fainter than given by Sirianni et al. (2005).

Not all GCs in the ACS Survey catalog will be considered in the analysis performed in the following sections. ω Cen (NGC 5139) and M 54 (NGC 6715) have been excluded because their complex CMDs and abundances indicate that these objects are not GCs in the traditional sense. Siegel et al. (2007) analyzed the M 54 CMD and measured ages for the stellar populations present and also estimated the metallicities of the stellar populations for which no spectroscopic information was available. Because M 54 lies at the center of the Sagittarius dwarf galaxy, it is not a simple process to distinguish between the stellar population(s) that belong to M 54 and those of the Sagittarius dwarf galaxy. ω Cen has long been known to contain a range of different metallicities as well as multiple stellar populations in the CMD (Lee et al. 1999). Johnson et al. (2008) presented a spectroscopic analysis of 180 red giants in ω Cen that revealed at least four distinct metallicities and a total range of ~ 1.5 dex in [Fe/H]. Other GCs for which multiple stellar population evidence exists will be noted

in the following sections. Piotto (2009) provided a summary of the GCs known to exhibit multiple stellar populations in their CMDs circa 2008. Three more GCs were excluded: Pal 1 and E 3 for lack of identifiable HB stars and Pal 2 due to extreme differential reddening (see Paper I). In total, 60 GCs from the ACS Survey are considered in the following analysis.

2.2. The six most distant GCs

The ACS Survey provides coverage of the Galactic GC population out to ∼20 kpc. In order to give proper consideration to the outer Galactic halo, where the second parameter phenomenon is most pronounced, the sample was extended to include the following GCs: NGC 2419 (Harris et al. 1997; Sandquist & Hess 2008); Pal 3, Pal 4, and Eridanus (Stetson et al. 1999); and AM-1 and Pal 14 (Dotter et al. 2008b). These are the six most distant GCs in the Galaxy with $70 \lesssim R_{GC} \lesssim 120$ kpc (Harris 1996). Unfortunately, no photometry of comparable quality is currently available for the 10 or so GCs that lie between these two groups ($25 \lesssim R_{GC} \lesssim 50$ kpc)[4]. In order to distinguish between the homogeneous ACS Survey sample and the larger, heterogeneous sample, the statistical analysis in section §5 will be presented with and without the six outer halo GCs.

2.3. Additional GC parameters

In addition to HB morphologies (§3) and ages (§4), several GC parameters were extracted from Mackey & van den Bergh (2005). The Mackey & van den Bergh (2005) catalog is based on the Harris (1996) catalog but includes several updated quantities and, importantly, provides quantities in absolute physical units. These units are more appropriate for comparisons than the observational units given in the Harris (1996) catalog. The quantities obtained from the Mackey & van den Bergh (2005) catalog are: Galactocentric distance (R_{GC}), integrated absolute V magnitude (M_V), half-light radius (R_h), and tidal radius (R_t). From the Harris (1996) catalog we extracted central luminosity density (ρ_0). Neither catalog includes basic measurements for Lyngå 7. Inclusion of these quantities in the following analysis makes it possible to explore the possibility that a GC's location in the Galaxy, structural properties, and total mass (assuming the mass-to-light ratio is constant) can influence its HB morphology.

[4]Pal 2 is one of these, and part of the ACS Survey catalog, but its CMD is so obscured by differential reddening that no useful information can be extracted from it (see Paper I). We note that during HST Cycle 17, GO 11586 will use ACS to image three GCs at $R_{GC} \sim 40$ kpc: Pal 15, NGC 7006, and Pyxis.

3. Measuring HB morphology

In this study, HB morphology is characterized by the difference between the median color of the HB stars and the median color of the RGB at the level of the HB, denoted $\Delta(V-I)$. This metric is essentially the same as d_{B-V} (Sarajedini 1999) and is less likely to become saturated than the most frequently used HB morphology parameter, (B−R)/(B+V+R) introduced by Lee (1989). As a corollary, the magnitude level of the HB in $F606W$ has also been measured; it provides a reference for GC distance estimates as discussed below.

3.1. The mean magnitude level of the HB

The mean level of the horizontal part of the HB was measured from the ACS Survey data relative to the HB of M 5 (NGC 5904). M 5 has a well-populated HB that extends approximately 0.7 mag in $F606W-F814W$ from the red side to the blue and, therefore, can overlay the HB of almost any other GC. Measurements were made by matching the CMD of each GC to that of M 5 in the region of the HB by making vertical and horizontal adjustments to the comparison CMD until it most closely overlaid that of M 5. In the majority of cases, the comparison GC had enough overlap to make the best alignment unambiguous. A few clusters with purely blue HBs, such as NGC 6254, present some difficulty because even the reddest HB stars do not become 'horizontal'. The measured HB levels are listed in Table 1. Typical measurement uncertainties are ∼0.05 mag and are dominated by the uncertainty inherent in aligning the HBs. The formal photometric errors of most HB stars are a few thousandths of a magnitude. The uncertainty is larger in cases where differential reddening is significant or the HB is otherwise difficult to quantify. As an example, Figure 1 shows HB levels for NGC 1261 and M 92 (NGC 6341).

3.2. The color difference, $\Delta(V-I)$

Measurements were obtained by drawing an outline around the HB and the RGB at the level of the HB and then calculating the statistics of the stars within each outline. This process is illustrated in Figure 1 for two GCs, NGC 1261 and M 92. RR Lyrae stars are not given special consideration in this analysis: they are included if they are present in the ACS observations. For the ACS Survey data, all determinations of HB membership were performed in the ACS $F606W-F814W$ CMD as shown in Figure 1. In order to allow direct comparison with GCs observed in different bands, the color difference presented in Table 1 is given in terms of $V-I$ rather than $F606W-F814W$. This was achieved by transforming

the ACS magnitudes of each individual HB star into V and I using the equations provided by Sirianni et al. (2005) and then calculating the median $V-I$ values of the HB and RGB. The median was chosen to represent the central tendency of $\Delta(V-I)$ because the HB stars are not normally distributed in color space. Hence, the more commonly-used mean and standard deviation are not the most appropriate choices. If the HB stars were normally distributed in color space, then the mean and median would be equal. In fact, about one half (one quarter) of the GCs in the sample have means and medians that differ by more than 5% (10%). For GCs with intermediate HBs, such as M 3 and NGC 1261, the mean and median are substantially different.

Table 1 provides the quantities used to determine $\Delta(V-I)$. In addition to the median $V-I$ of the HB and RGB, 1-σ errors on these quantities are listed and the quadrature sum is given as the uncertainty on $\Delta(V-I)$. Uncertainty in the median $V-I$ was estimated by bootstrapping with replacements performed 10,000 times on both the HB and RGB of each GC. The error bars on the median represent the range of $V-I$ within which 68% of bootstrapped medians lie. To compliment the median and uncertainty, we also give the mean absolute deviation (MAD) for the HB and RGB. The mean absolute deviation represents the intrinsic spread in each individual data set. Consider, for example, the HBs of 47 Tuc (NGC 104) and M 3 (NGC 5272). Both have well-populated HBs and thus small uncertainties, $\sigma < 0.01$ determined from bootstrapping, but 47 Tuc has a tightly clustered red clump of HB stars and a small MAD=0.023 while M 3 has a more broadly distributed HB and a larger MAD=0.208.

3.3. Comparison with other HB morphology parameters

Perhaps the most frequently used HB morphology metric in the literature is (B−R)/(B+V+R): the difference between the number of blue HB stars (B) and the number of red (R) normalized by the total number of HB stars including variables (V). Its major inconvenience is that it saturates if all stars lie on one side or the other of the instability strip. The left panel of Figure 2 compares (B−R)/(B+V+R) from Mackey & van den Bergh (2005) and $\Delta(V-I)$ from this paper for the 66 GCs in the present sample. There is an obvious correlation between the two but $\Delta(V-I)$ continues to vary after (B−R)/(B+V+R) saturates.

The most recent large-scale study of HB morphology, that of Recio-Blanco et al. (2006), used the maximum effective temperature encountered along the HB [Log $T_{\rm eff}$(HB)] determined with the use of theoretical zero-age HB sequences from Cassisi et al. (1999). The Log $T_{\rm eff}$(HB) metric appears to be complimentary to $\Delta(V-I)$ or (B−R)/(B+V+R) because, while it lacks sensitivity through the middle, it is more sensitive at the extremes. This

is demonstrated in the right panel of Figure 2. In the absence of an ideal HB morphology metric that quantifies every feature of interest, it is beneficial to identify a metric that is well suited to a particular problem.

4. Globular cluster ages

4.1. Relative ages

Marin-Franch et al. (2009, Paper VII) presented relative ages measured from the ACS Survey data. These ages were derived by first measuring the absolute magnitudes of the main sequence turnoffs (MSTOs) for all GCs and then interpolating in isochrone-based grids of MSTO as a function of age and metallicity. The same analysis was performed with four different isochrone libraries and the distribution of relative ages with metallicity was shown to be independent of the isochrone library. For the purpose of the present paper, relative ages derived from Dotter et al. (2007, Paper II) isochrones using the Zinn & West (1984, hereafter ZW84) metallicity scale have been adopted. Furthermore, we assumed that GCs with [Fe/H] < -1 have [α/Fe]=+0.3 and GCs with [Fe/H] ≥ -1 have [α/Fe]=+0.2. The ages measured in this fashion and with these assumptions were placed on a relative scale by dividing out the average age of the most metal-poor GCs ([Fe/H] < -1.8), in this case 13.3 Gyr. In the present study, this factor has been retained, resulting in absolute ages for the particular isochrone library, metallicity scale, and method of age determination employed in Paper VII.

4.2. Isochrone fitting

In order to put the ACS Survey ages on the same scale as the six outer halo GCs, and to demonstrate that later results do not depend on the method used, age estimates were determined using isochrone fitting to the CMDs of all GCs in the data set. The fits were performed using isochrones from Paper II for the ACS Survey data and Dotter et al. (2008a) for the outer halo GCs. The same zeropoint corrections applied to the ACS data, as described in §2.1, were applied to the isochrones in the ACS photometric system as well. The underlying luminosities, temperatures, surface gravities, and color transformations of the isochrones in Paper II and Dotter et al. (2008a) are identical. The only difference between the two is the photometric system. The outer halo GCs were measured in $F555W$ and $F814W$, whereas the ACS Survey data were taken in $F606W$ and $F814W$. Several GCs were excluded from isochrone fitting because they are known to harbor multiple stellar

populations. The presence of more than one stellar population makes a single age determination insufficient to characterize the GC. Ages were not determined for the following GCs: NGC 1851 (Milone et al. 2008, Paper III), NGC 2808 (Piotto et al. 2007), NGC 6388, NGC 6441[5], and NGC 6656 (Piotto 2009).

It is likely that other GCs with multiple populations exist, even within the ACS Survey data, but to have avoided detection thus far the separation between the populations must either be so small that they overlap to a great extent or that reddening has obscured the separation in the CMD. A second population may also represent a small fraction of stars and have little or no apparent influence on the HB morphology. The recent discovery of a second subgiant branch in 47 Tuc (NGC 104) by Anderson et al. (2009) is an example: this second population accounts for only $\sim$10% of the stars in the core. Further out, the CMD was too sparsely populated to detect this population. It should also be noted that Anderson et al. (2009) found the main population of 47 Tuc to have a spread in the CMD greater than can be accounted for by the photometric errors. The authors found it unlikely that this spread was due to binaries, differential reddening, or a depth effect. Anderson et al. (2009) explored the possibility that the color spread could be caused by an intrinsic variation in the He abundance or [Fe/H]. Another case is M 4 (NGC 6121). Marino et al. (2008) presented spectroscopic evidence for a bimodal abundance distribution along the RGB of M 4 as well as a broadening of the RGB in $U-B$. Whether M 4 contains two distinct stellar populations or a continuous distribution is not clear at present. If it is the former, the difference is small enough to remain undetected on the main sequence in the exquisite photometry presented by Bedin et al. (2009). If it is the latter, age determinations are expected to be reasonable (see the discussion at the end of §4.3).

The procedure used to determine ages involved a two step process. Initial estimates for [Fe/H], distance modulus, and reddening estimates were taken from the Harris (1996) catalog, 2003 revision. Estimates of [α/Fe] were chosen as appropriate for a given value of [Fe/H]. All efforts were made to follow these values as closely as possible with minor adjustments made to improve the fit to the unevolved main sequence first and the RGB second. In some instances, isochrones at the catalog values were not able to provide an adequate fit to the CMDs and, in these cases, the initial estimates of [Fe/H], distance, and reddening were allowed to vary until the fit obtained was acceptable. This step was a necessity in a number of cases because the published values for some lesser-known GCs are uncertain.

[5]Given the great similarities between the CMDs of NGC 6388 and NGC 6441 we have chosen to exclude both although Piotto (2009) only showed evidence for multiple populations in NGC 6388.

For example, Dotter et al. (2008b) found that the main sequence and RGB morphologies of AM-1 are comparable to those of M 3 although the former is listed at [Fe/H] = −1.8 while the latter is listed at [Fe/H] = −1.57 in the Harris catalog. Another example is the distance modulus of NGC 6254: the Harris catalog value is $DM_V = 14.08$ but the present study produces a value that is ∼0.2 mag fainter. This result is confirmed by both isochrone fitting to the main sequence and the level of the HB from Table 1. These results are not meant to diminish the value of the GC catalogs, which are invaluable resources, but merely to emphasize that there are still many GCs in the Galaxy whose properties are poorly constrained. The models, which are homogeneous in terms of physical assumptions and ingredients, can prove useful in determining the relative differences between two GCs if one has well-measured properties and another does not.

Several of the GCs in the ACS Survey are heavily obscured by interstellar reddening. Differential reddening confuses the age determinations in such GCs because the reddening line is nearly perpendicular to the most age-sensitive features: the main sequence turnoff and the subgiant branch. Differential reddening causes these features to be spread out and, in light of this trend, we have attempted to correct for its effects in the following manner. The first step involves the construction of a fiducial sequence for the GC. The fiducial sequence is centered approximately at the MSTO. More stars lie below the MSTO than above but the differential corrections are weighted based on the angle between the stellar sequence and the reddening line. Since the reddening line is almost perpendicular to the subgiant branch, the differential correction is approximately equally weighted by stars above and below the MSTO. Care is taken to avoid unresolved binaries. From the fiducial sequence, each individual star yields a color residual, taken along the reddening direction in the CMD. From these residuals a reddening map is created by finding the median residual in each 256×256 pixel square of the image. Then each star is corrected, along its reddening line, by an amount that is interpolated from the 16×16 points of the reddening map. A full explanation of these procedures, the differentially corrected CMDs, and reddening maps will be provided in a forthcoming paper (I. King, 2009, in preparation).

The best-fit age of a given GC was estimated by determining the isochrone that best fit the CMD from the MSTO through the subgiant branch. The uncertainty was derived from the intrinsic scatter in the CMD and/or the inherent mismatch between the models and the data. The range of ages that allowed the isochrones to envelope the bulk of the stars at the MSTO and on the subgiant branch are taken to be 1-σ uncertainties. The age uncertainty is only based on the fitting procedure described and does not account for uncertainties in the input physics of the stellar models or differences between the chemical composition assumed in the models and those actually present in the stars (for more on this point, see §4.3). Hence the uncertainties include the random component but exclude the systematic. Still, it

is worthwhile to consider that incomplete knowledge of chemical composition and incomplete treatment of the physics, such as rotation and convection, in the current generation of 1-D stellar evolution models are primary sources for the systematic error present in the analysis.

The results of isochrone fitting are listed in Table 2. If a differential reddening corrected CMD was employed in the fit, an asterisk (*) appears after the name in Table 2. Figures 3 through 5 demonstrate how the isochrone fits were achieved for three different GCs. Figure 3 shows a case where the isochrones trace the stellar population throughout the CMD (left panel) and how the age, 12.5±0.5 Gyr, was measured (right panel). Figure 4 shows the differential reddening-corrected CMD of NGC 3201. The corrected CMD reduces the scatter about the subgiant branch but the age uncertainty is still larger than in the case of NGC 6362. Figure 5 shows the worst case scenario where the reddening is low and the isochrones match the unevolved main sequence and RGB but not the shape of the age sensitive region. The slope of the models is shallower than the data along the subgiant branch and, although the data define a narrow sequence, the age is poorly constrained. This case is likely to be severely affected by the systematic errors described in the preceding paragraph.

As a consistency check, it is useful to plot the absolute magnitude of the HB as a function of metallicity. The absolute magnitude of the HB is obtained by subtracting the $F606W$ distance modulus derived from the isochrone fits (Table 2) from the apparent magnitude of the HB (Table 1). The resulting quantity is plotted in Figure 6 for the ACS Survey clusters. The points define a relatively tight relationship. A linear, least squares fit to these data for GCs with [Fe/H] ≤ -1 gives:

$$< M_{F606W}(HB) >= (0.227 \pm 0.011)[\mathrm{Fe/H}] + 0.802 \pm 0.020, \quad (1)$$

which is shown as the solid line in Figure 6. The quoted errors in equation (1) are due only to scatter in the data and do not include measurement uncertainties. The fit is limited to clusters with [Fe/H] ≤ -1 so as to exclude clusters with predominantly red HB morphologies. The justification for restricting the fit is that red HB GCs often lack RR Lyrae variable stars. Some GCs with completely blue HBs were included in the fit even though they may not have RR Lyrae stars. As described in §3.1, the uncertainty in the apparent magnitude of the HB is approximately 0.05 mag per GC and this is shown by the two dashed lines. All but a handful of points lie within the dashed lines.

If equation (1) is transformed from $F606W$ to V using the synthetic color transformations employed in Paper II, the slope increases by $\lesssim 0.01$ because of a very slight metallicity dependence of $V - F606W$ on [Fe/H] and, assuming a characteristic temperature for RR Lyrae stars of LogT=3.83, the intercept increases by 0.09 mag. Chaboyer (1999) gave $M_V(RR) = (0.23\pm0.04)([\mathrm{Fe/H}]+1.6) + (0.56\pm0.12)$. Other recent estimates include

$M_V(HB)$=(0.22±0.05)([Fe/H]+1.5)+(0.56±0.07) (Gratton et al. 2003) and a further refinement of the slope to 0.214±0.047 mag/dex (Gratton et al. 2004). If equation (1) is transformed again so that the independent variable is ([Fe/H] + 1.6) and the dependent variable is M_V rather than M_{F606W}, it becomes $M_V(HB) = 0.235([\mathrm{Fe/H}] + 1.6) + 0.53$ where the error bars have been omitted for brevity. The relationship between $M_V(HB)$ and [Fe/H] derived here is within the 1-σ uncertainties from each of the three determinations previously mentioned.

4.3. Metallicity scales and chemical abundance variations

Figure 7 compares [Fe/H] from Table 2 and the ZW84 scale with the Kraft & Ivans (2003, hereafter KI03) scale for 47 GCs in common between KI03 and this paper. (KI03 provided [Fe/H] values measured with three different model atmospheres; this paper adopts their measurements based on MARCS models.) For reference, the line of equality is drawn on both panels of Figure 7. Paper VII compared ages on the ZW84 and Carretta & Gratton (1997, hereafter CG97) scales. As discussed by KI03, the CG97 scale is consistently higher than either the ZW84 or KI03 scales, by 0.2-0.3 dex in general. It is beyond the scope of this paper to determine which scale is superior to the others[6]. Suffice it to say that ages and metallicities from Table 2 and Paper VII on the ZW84 scale will be used in the analysis that follows. However, speaking hypothetically, if it is assumed that the KI03 scale is the 'correct' [Fe/H] scale, then the residuals from the solid line in each panel of Figure 7 can be interpreted as uncertainties in the adopted scales. We shall return to this hypothesis in §5.1.

The ages reported in Tables 4 are based on isochrones that assume an α-enhanced composition. They do not explicitly account for variations in the He or C+N+O abundances but, if such variations are present, they should certainly influence age determinations (Ventura et al. 2009; D'Antona et al. 2009). While the extent of He and C+N+O variations in GCs are largely unknown at present, the existence of light element abundance variations is quite clear. The review by Gratton et al. (2004b), the recent results presented by Carretta et al. (2009a,b), and many other studies have shown the widespread presence of chemical abundance variations within individual GCs. These abundance variations are among the light elements (C, N, O, Na, Mg, and Al) and do not extend to heavier elements such as Fe in the majority of GCs. Models for GC self-enrichment predict that varying

[6] Recently, Carretta et al. (2009c) presented a new GC metallicity scale based on the largest spectroscopic survey of GC red giants to date. The analysis reveals a very close agreement between the new metallicity scale and that of KI03. This is in spite of the fact that KI03 used Fe II lines while Carretta et al. (2009c) relied on Fe I lines. On the other hand, the new scale is consistently ∼0.2 dex lower than that of CG97.

degrees of He variation should accompany the other abundance variations (D'Antona et al. 2002; Decressin et al. 2007). The influence of such abundance variations on GC ages is not fully understood at present. However, the recent results from Carretta et al. (2009a,b) lend some insight into the problem of deriving GC ages in the presence of light element abundance variations. Those authors identify three groups of stars within GCs based on their chemistry. They are: the 'primordial' stars or stars which have halo-like abundances, characterized by super-solar O and sub-solar Na; the 'intermediate' stars, with slightly less O and more Na than the primordial stars; and the 'extreme' stars, characterized by [O/Na] < -0.9. Carretta et al. (2009a,b) state that all GCs (measured so far) contain primordial and intermediate stars but not all GCs contain the extreme component. Furthermore, the majority of GC stars are in the intermediate group.

How do these findings influence GC age estimates? Pietrinferni et al. (2009) compared stellar evolution models from the BaSTI library (Pietrinferni et al. 2004, 2006) with chemical compositions representative of the primordial and extreme groups. Pietrinferni et al. (2009) state that, as long as the total amount of C+N+O remains constant, it is safe to use α-enhanced isochrones to derive GC ages. However, if the total amount of C+N+O varies among the stars in a given GC, then it is necessary to use models with the appropriate CNO abundances to derive GC ages. This is all without consideration of a potential change in the He content that is predicted to accompany the light element abundance variations. The He abundance is important because models of chemical enrichment in GCs predict that the abundance variations from the primordial values should be accompanied by an increase in He, whether the source of the enrichment is massive stars (Decressin et al. 2007) or intermediate mass AGB stars (D'Antona et al. 2002). The extreme stars should be most He-enriched, the intermediate stars should be slightly He-enriched, and the primordial stars should have primordial He. Salaris et al. (2004) investigated the He content of 57 GCs using the R parameter: the ratio of the number of HB stars to the number of RGB stars brighter than the HB. Within the uncertainties, they found little or no evidence for a spread in the He content of GCs with (B−R)/(B+V+R) < 0.8. For GCs with (B−R)/(B+V+R) ≥ 0.8, Salaris et al. (2004) found a larger spread and a tendency toward higher He abundances. These authors state that the apparent trend towards higher He abundances in GCs with blue HBs may be related to increased evolutionary timescales for the lowest mass HB stars not entirely accounted for in their calibration of the R parameter or the genuine presence of He-rich stars in the blue HBs of some GCs. As long as the total metal content remains constant, a modest spread ($\Delta Y \lesssim 0.05$) in the He content of a GC will not significantly alter the level of the main sequence turnoff or subgiant branch (Dotter et al. 2009) and therefore not confuse the age determination. If the total metal content varies or the spread in He is larger, age estimates will require great care and detailed abundance information. It is

important to keep in mind the complexities of measuring GC ages in the context of chemical abundance variations–and their proposed origins–in GCs.

4.4. Age-Metallicity Relations

The average difference between the ages derived in §4.2 and in Paper VII is −0.104 Gyr; the standard error of the mean is 0.105 Gyr and the standard deviation is 0.781 Gyr. Figure 8 shows the normalized age differences of 56 GCs. The age differences are calculated by subtracting the Paper VII age from the age listed in Table 2 and dividing by the quadrature sum of the age uncertainties from both sources. In accordance with Paper VII, metallicity is represented in Figure 8 and later figures by [M/H]=[Fe/H]+$\mathrm{Log}_{10}(0.638 \times 10^{[\alpha/\mathrm{Fe}]} + 0.362)$ (Salaris et al. 1993). The ages of 43 of the 55 GCs shown in Figure 8 differ by less than 1-σ. The primary reason for disagreement in ages is most likely the adopted metallicity scale since the largest systematic deviation occurs around [M/H]~ -1 and the metallicity scales deviate there by as much as 0.3 dex (see Figure 7).

Figure 9 compares the AMRs from this paper with those of Paper VII (top panel) and VandenBerg (2000) (bottom panel). Despite the age differences already addressed in Figure 8 and the preceding paragraph, both AMRs reveal the same general features. The main difference is that the ages from Table 2 show smaller dispersion at low and high metallicities. The appearance of a separate trend beginning at [M/H]=−1.5 and extending to Pal 12 and Ter 7 (the two youngest GCs) is nearly identical in both AMRs. The open circles in the upper panel are the outer halo GCs not present in the ACS Survey data; these additional GCs strengthen the trend already present in the ACS Survey data. Given that VandenBerg (2000) carried out his analysis using a heterogeneous collection of data in $B-V$ and $V-I$, and used distances set by the level of the HB, it is encouraging that all three AMRs reveal the same basic trends.

5. Results & Analysis

5.1. $\Delta(V-I)$ and the second parameter

HB morphology is most strongly influenced by the first parameter, metallicity. The metallicity-$\Delta(V-I)$ diagram is shown in Figure 10. For the ACS Survey data, the inner halo GCs ($\mathrm{R_{GC}} \leq 8$ kpc) are plotted as circles and the outer halo GCs ($\mathrm{R_{GC}} > 8$ kpc) as squares. The six most distant GCs are plotted as triangles and only appear in the left panel because they were not considered in Paper VII. The left panel shows the metallicity scale

from Table 2 and the right panel shows the ZW84 metallicity scale from Paper VII. The error bars shown are only due to measurement errors in $\Delta(V-I)$ as listed in Table 1.

In order to more clearly identify the second parameter, an attempt was made to remove the influence of metallicity from the HB morphology data, thereby exposing the second parameter effect. To accomplish this, a function was fit to the inner halo GCs which cover the full range of metallicity and exhibit relatively little scatter in the [M/H]-$\Delta(V-I)$ diagram, with the notable exception of NGC 6584. NGC 6584 is presently located at $R_{GC} \sim 7$ kpc but Lee et al. (1994) noted its position in the metallicity-HB morphology diagram and large, positive heliocentric velocity and suggested it is actually an outer halo GC. This suggestion is supported by Dinescu et al. (1999) who calculated its apogalacticon at 12.6 ± 2.4 kpc. As a result, M 5 (see §1) and NGC 6584 were excluded from the fit. The fitting function is made up of two parts with x=[M/H],

$$\Delta(V-I)_{fit}(x) = f(x) + g(x). \tag{2}$$

The first part, f, resembles a Fermi-Dirac function that transitions from blue to red as metallicity increases, as suggested by Catelan (2009). The second part, g, is a quadratic that allows for the remaining curvature, in particular that the most metal-poor GCs turn back to the red with decreasing metallicity as can be seen in Figure 10. The two parts are

$$f(x) = a_0 - a_1 \left[\frac{exp\left(\frac{x+a_2}{a_3}\right)}{1 + exp\left(\frac{x+a_2}{a_3}\right)} \right] \tag{3}$$

and

$$g(x) = b_0 + b_1\ x + b_2\ x^2. \tag{4}$$

The a's and b's were determined from a least squares fit. For comparison, and to demonstrate the robustness of the method, the same functional form was fit to the inner halo $\Delta(V-I)$ data using the metallicity scale from Table 2 (shown in the left panel of Figure 10) and the ZW84 metallicity scale from Paper VII (right panel). The fitting function coefficients are reproduced in Table 3.

The search for correlations focuses on the difference between the measured $\Delta(V-I)$ of an outer halo GC and the $\Delta(V-I)$ value of the inner halo trend (as represented by the fitting function) at that GC's metallicity. This quantity will henceforth be referred to as $\Delta(\mathrm{Fit} - \mathrm{Measured})$. Figure 11 shows how $\Delta(\mathrm{Fit} - \mathrm{Measured})$ varies with metallicity; the symbols are the same as in Figure 10. With the exception of NGC 6584 the inner halo GCs exhibit residuals of $\sim$0.1 or less. Altogether, metal-rich GCs ([M/H]$\gtrsim -0.8$) show very little scatter in Figure 11. Evidently, metallicity alone is almost sufficient to describe the HB

morphology of the majority of metal-rich GCs and thus they are of little use in the search for the second parameter. The solid error bars shown in Figure 11 represent the measurement errors listed in Table 1.

Metallicity uncertainty plays an important role in this diagram and thus the error bars in Figure 11 are only a lower limit to the total uncertainty in $\Delta(V-I)$. Unfortunately, it is not possible to provide realistic metallicity errors for all of the GCs in the sample. For the large deviation shown for $-1.5 < [\mathrm{M/H}] < -1$ in Figure 11 to be completely erased, metallicities of the GCs in this region that stand out would have to be systematically underestimated by 0.25-0.5 dex. Such a conspiracy seems highly unlikely. However, it is possible to approximate the effect of metallicity errors on $\Delta(V-I)$ in the following manner. First, the fitting function described by equations 3 and 4 was applied to the inner halo GCs with metallicities on the KI03 scale. Next, the KI03-based fitting function was used to calculate a $\Delta(V-I)$ but using the metallicity from Table 2 or the ZW84 scale, thereby introducing a metallicity error. Finally, the difference between the erroneous $\Delta(V-I)$ value obtained in this manner and the value obtained from the appropriate fitting function provides an estimate of how a metallicity error propagates into a $\Delta(V-I)$ error.

Under the hypothesis that the KI03 [Fe/H] scale is the 'correct' one, this procedure gives an indication of how a metallicity error (a vertical displacement in Figure 10) influences the significance of the distance between a GC and the inner halo fitting function (the horizontal distance between a point and the fit line in Figure 10) which we refer to as $\Delta(\mathrm{Fit}-\mathrm{Measured})$. The dashed error bars in Figure 11 are the quadrature sum of the $\Delta(V-I)$ measurement errors from Table 1 and the metallicity errors estimated as described in the preceding paragraph. The metallicity effect is small except in the vicinity of the transition from red to blue that occurs around $[\mathrm{M/H}] \sim -1$ (see Figure 10) where a small change in metallicity corresponds to a large change in $\Delta(V-I)$. It should be stressed that this approach is not a rigorous treatment of the influence of metallicity uncertainty on $\Delta(V-I)$ or $\Delta(\mathrm{Fit}-\mathrm{Measured})$ because it assumes the difference between one scale and another is the error. Nevertheless, it serves to illustrate that the existence of several GCs with $-1.5 \lesssim [\mathrm{M/H}] \lesssim -1$ and large, positive values of $\Delta(\mathrm{Fit}-\mathrm{Measured})$ cannot readily be attributed to metallicity errors alone.

Figures 12 through 17 show how the $\Delta(V-I)$ difference depends on $\mathrm{R_{GC}}$, M_V, $\mathrm{R_h}$, $\mathrm{R_t}$, ρ_0, and age for the outer halo GCs. In order to quantify the information provided in the plots, Spearman's rank correlation coefficient was calculated for the data presented in Figures 12 through 17 and included in the figures. The Spearman rank correlation coefficient (Spearman's ρ) measures the degree of correlation between two variables but makes no assumption about the functional form of their relationship other than monotonicity. As

such, it is a very general measure of correlation; a perfect correlation has a value of $\rho = +1$, a perfect anti-correlation has $\rho = -1$, and complete lack of correlation has $\rho = 0$. The left panels show the 6 most distant GCs, which were not part of the ACS Survey, as triangles. Since these 6 GCs are not part of the homogeneous ACS data set, and were not considered in Paper VII, we have calculated the Spearman correlation coefficients with and without them in the left panels. Apart from NGC 2419, the other 5 most distant GCs tend to strengthen the correlation coefficients because they are more distant, intrinsically fainter, more extended, and younger.

$\Delta(V-I)$ error bars are included in Figures 10 through 17, and age errors in Figure 17, but uncertainties in the other quantities are neither readily available nor simple to estimate given the wide range of distances and reddenings present in the sample. It is, however, important to consider that the quantities in Figures 12 through 16 were converted to physical units after adopting a particular distance modulus. As distance increases, a given error in the distance corresponds to a larger uncertainty in the physical quantity.

While R_{GC}, M_V, R_h, R_t, and ρ_0 reveal no obvious visible trends, Figure 17 shows a trend with age. The Spearman coefficients support this conclusion: M_V, R_h, R_t, and ρ_0 show no strong correlations. R_{GC} shows a mild correlation but that is mostly likely due to a large anti-correlation between age and R_{GC}. Age shows a significant anti-correlation and the age trend works as anticipated: the HBs grow redder with decreasing age and so the distances between the measured $\Delta(V-I)$ values and the inner halo trend increase as age decreases. The results presented in this section demonstrate that, of all the parameters considered here, age has the most significant correlation with $\Delta(\mathrm{Fit}-\mathrm{Measured})$.

Figure 17 and the accompanying slopes and coefficients do not include Pal 12 or Terzan 7, the two youngest GCs in the sample. Both GCs are metal rich and so their HB morphologies are almost entirely determined by their metallicity alone. The presence or absence of Pal 12 and Ter 7 does not significantly alter the correlation coefficients ($\delta\rho \lesssim 0.05$) for any of the other quantities. Figure 17 also includes a linear fit to each data set that describes the rate at which HB morphology varies with age. The ages and metallicities listed in Table 2 suggest that HB morphology changes over a smaller age interval than those from Paper VII, but only by about $\sim$0.5 Gyr. The larger errors that include the metallicity effect were not used in the least squares fits to the age-$\Delta(\mathrm{Fit}-\mathrm{Measured})$ relations shown in Figure 17. If they had been, the slope of the relation derived using the Paper VII ages (shown in the right panel) would be reduced to -0.21 ± 0.05 while the slope derived from the ages given in Table 2 would not change significantly.

5.2. A possible third parameter

In §5.1, it was shown that when the inner halo relationship between metallicity and $\Delta(V-I)$ is subtracted from the outer halo GCs, a correlation between age and $\Delta(\mathrm{Fit}-\mathrm{Measured})$ appears. The inner halo GCs were chosen to define the trend because they exhibit a tight relation with little scatter in the HB morphology–metallicity diagram (Searle & Zinn 1978, see also Figure 10 in this paper). Unfortunately, attempts to use this technique a second time–to subtract off the age trend–were unsuccessful because the remaining residuals are generally smaller than the measurement uncertainties in $\Delta(V-I)$. Thus, to identify a potential third parameter, it is necessary to remove the effect of metallicity and age to the fullest extent possible. The most metal poor GCs ($[\mathrm{M/H}] < -1.5$) in the sample are an ideal choice because they have a small range in ages (§4) and only a weak metallicity dependence on HB morphology (see Figure 10).

Comparisons of the metal poor GCs' $\Delta(\mathrm{Fit}-\mathrm{Measured})$ values with M_V, $\mathrm{R_h}$, $\mathrm{R_t}$, and ρ_0 were performed. Of these, central density (Log ρ_0) produced the most significant trend. Figure 18 demonstrates how central density relates to $\Delta(\mathrm{Fit}-\mathrm{Measured})$ among the metal poor GCs using the two fitting functions employed in §5.1 and the same symbols used in Figures 10 through 17. There is an evident trend with the highest central density GCs having the bluest HB morphologies and hence the smallest $\Delta(\mathrm{Fit}-\mathrm{Measured})$ values. Assuming that the contributions of age and metallicity are minimal in Figure 18, the influence that central density has on HB morphology in the metal poor GCs is evident and its magnitude is ~ 0.2 in $\Delta(\mathrm{Fit}-\mathrm{Measured})$. Although it is difficult to disentangle the effects of age and central density in GCs with intermediate metallicities ($-1.5 < [\mathrm{M/H}] < -1$), where the second parameter is most pronounced, these GCs span essentially the same range of central densities as the metal poor GCs. Thus central density should only account for a small portion of the HB morphology variation seen in the intermediate metallicity group. The influence of central density on HB morphology has already been demonstrated by Fusi Pecci et al. (1993), Buonanno et al. (1997), and Smith (2004). However, its effect is not as pronounced as that of age (compare Figures 17 and 18). Therefore central density is the most likely candidate for the third parameter influencing HB morphology (as characterized by $\Delta(V-I)$) that has been considered by this study.

5.3. Discussion and comparisons with previous results

It is worthwhile to demonstrate that the use of the inner halo GCs to define the HB morphology–metallicity relation does not include an unintended bias. In particular, since claims have been made in the preceding sections that, after metallicity, age and central

density are the two most significant factors influencing HB morphology [as represented by $\Delta(V-I)$], it is important to demonstrate that the HB morphology–metallicity trend derived from the inner halo GCs does not include an implicit dependence on either of these quantities. Indeed, as Figure 19 shows, the inner halo GCs exhibit some dispersion inside 8 kpc in both central density (left panel) and age (right panel) but there is no clear, systematic variation of either parameter as a function of R_{GC} inside 8 kpc (denoted by the dotted line in the figure).

Figure 10 demonstrates that the HB morphologies of the inner halo GCs, which have a fairly homogeneous age distribution, transition from blue to red as [M/H] rises through ~ -1. The metal rich GCs have red HBs (though NGC 6388 and NGC 6441 also have blue extensions) while the majority of metal poor GCs have blue HBs. It is at metallicities that are lower than, but within a few tenths of a dex of, [M/H]=−1 where a GC is most likely to move a large distance in the $\Delta(V-I)$–metallicity diagram due to a relatively small change in metallicity or another parameter. It is within this same narrow metallicity range that the AMR of the outer halo GCs branches off from that of the inner halo GCs (see Figure 9) and so it is no coincidence that the classic second parameter effect is most pronounced in the outer halo.

The analysis presented in §5.1 indicates that a GC with $-1.5 <$[M/H]< -1 requires 2-2.5 Gyr to transition from a red HB to a blue one. This result is consistent with a number of studies mentioned in the introduction. We confirm the assertion by Lee et al. (1994) that the presence of metal poor GCs with red HBs at large R_{GC} is primarily an age effect. However, our result indicates that Lee et al.'s claim that the necessary age difference is greater than ∼3 Gyr is slightly exaggerated[7]. That a GC with $-1.5 <$ [M/H] < -1 transitions from a red to a blue HB in 2-2.5 Gyr poses a challenge to our understanding of mass loss during the red giant phase of evolution. RGB mass loss has been essentially a free parameter in synthetic HB models since they were first constructed by Rood (1973). A number of mass loss rates that vary as a function of global stellar properties such as luminosity, mass, radius, or some combination of the three have been proposed with varying degrees of success, see Catelan (2009) for a detailed discussion. Following Lee (1991), Dotter (2008) showed that a simple relationship between global metallicity and average RGB mass loss, along with stochastic variations, can reproduce the general trend observed in old, roughly coeval Galactic GCs in the HB morphology-metallicity diagram. Recent progress from observations by, e.g. Origlia et al. (2007), McDonald et al. (2009), Mészáros et al. (2009), and Dupree et al.

[7]It is important to keep in mind that there is a small, but not insignificant, number of GCs with younger ages, such as Pal 1 (Paper I), Pal 12, and Ter 7; these tend to be metal rich and so their HB morphologies are governed almost entirely by metallicity.

(2009), should lead to a better understanding of RGB mass loss as a function of composition, evolutionary status, and pulsational properties.

The recent, large-scale study of HB morphology by Recio-Blanco et al. (2006) suggests that, just as age can explain anomalously red HBs in some GCs, total GC mass is linked to the degree of abundance variation and the extent of the faint blue tail observed in other GCs. (Of course, there is no reason why both effects cannot be operating in the same GC.) Recall that Figure 2 showed the HB morphology metric adopted by Recio-Blanco et al. (2006) was very sensitive to the extremes but lacked sensitivity through the middle of the distribution. In the absence of an ideal HB morphology metric, a large-scale study of HB morphology should choose a metric that is well-suited to the effect(s) of interest to that investigation.

6. Conclusion

HB morphologies characterized by $\Delta(V-I)$ of 66 Galactic GCs were examined to determine the sensitivity of HB morphology to a variety of different factors. Deep, homogeneous photometry from the ACS Survey of Galactic GCs accounts for 60 of these while the remaining 6 GCs are the most distant Galactic GCs known. The complete sample is the largest examined to date and consists solely of high-quality HST photometry. It spans the full range of R_{GC} and almost the entire range of metallicity present in the Galactic GC population. $\Delta(V-I)$ values and two independently measured sets of ages were joined with other quantities from the literature to assess the relative importance of these quantities on HB morphology.

The data were split into two groups, roughly equal in number, based on R_{GC}. The tight relationship between metallicity and HB morphology in the inner halo group ($R_{GC} < 8$ kpc) was characterized by a fitting function and this trend was subtracted off of the outer halo group. The difference between fit and measured $\Delta(V-I)$ was then compared to a variety of parameters, of which only age showed a significant correlation. The age correlation does not rely on the presence of the 6 most distant GCs in the analysis, though their presence does strengthen the result. Hence we conclude that, after metallicity, age has the most influence on $\Delta(V-I)$. The age spread among the bulk of GCs in the Galactic halo was found to be 2-2.5 Gyr, though there are a few younger outliers such as Pal 12 and Ter 7. Further analysis, in which both metallicity and age were restricted, provided strong evidence that central luminosity density (ρ_0) is the third most influential parameter on $\Delta(V-I)$.

We wish to express our gratitude to the anonymous referee for a thoughtful, thorough report that improved the accuracy and focus of the paper. We thank Ivan King for sharing

his differential reddening corrected CMDs in advance of publication and the following people for sharing their HST photometry: Peter Stetson (Pal 3, Pal 4, and Eridanus), Bill Harris (NGC 2419), and Eric Sandquist (NGC 2419). AD acknowledges support from a CITA National Fellowship and an NSERC grant to D. VandenBerg. Further support for this work (proposal number GO-10775) was provided by NASA through a grant from the Space Telescope Science Institute which is operated by the Association of Universities for Research in Astronomy, Incorporated, under NASA contract NAS5-26555.

REFERENCES

Anderson, J. et al. 2008, AJ, 135, 2055 (Paper V)

Anderson, J. Piotto, G., King, I. R., Bedin, L. R., & Guhathakurta, P. 2009, ApJ, 697, L58

Arp, H. C., Baum, W. A., & Sandage, A. R. 1952, AJ, 57, 4

Bedin, L. R., Salaris, M., Piotto, G., Anderson, J., King, I. R., & Cassisi, S. 2009, ApJ, 697, 965

Bellazzini, M., Fusi Pecci, F., Ferraro, F. R., Galleti, S., Catelan, M., Landsman, W. B. 2001, AJ, 122, 2569

Bohlin, R. C. 2007, Instrument Science Report ACS 2007-06

Bolte, M. 1989, AJ, 97, 1688

Buonanno, R., Corsi, C., Bellazzini, M., Ferraro, F. R., & Pecci, F. Fusi 1997, AJ, 113, 706

Buonanno, R., Corsi, C., Castellani, M., Marconi, G., Fusi Pecci, F., & Zinn, R. 1999, AJ, 118, 1671

Carretta, E., Bragaglia, A., Gratton, R., D'Orazi, V., & Lucatello, S. 2009c, A&Ain press (arXiv:0910.0675)

Carretta, E., Bragaglia, A., Gratton, R. G., & Lucatello, S. 2009b, A&A, 505, 117

Carretta, E. et al. 2009a, A&A, 505, 139

Carretta, E. & Gratton, R. G. 1997, 1997, A&AS, 121, 95 (CG97)

Carretta, E., Recio-Blanco, A., Gratton, R., Piotto, G., & Bragaglia, A. 2007, ApJ, 671, 125

Cassisi, S., Castellani, V., Degl'Innocenti, S., Piotto, G., & Salaris, M., 2001, A&A, 366, 578

Catelan, M. 2000,ApJ, 531, 826

Catelan, M. 2009, Ap&SS, 320, 261

Catelan, M., Bellazini, M., Landsman, W. B., Ferraro, F. R., Fusi Pecci, F., & Galleti, S. 2001, AJ, 122, 3171

Catelan, M & de Freitas Pacheco, J. A. 1993, AJ, 106, 1858

Catelan, M & de Freitas Pacheco, J. A. 1995, 297, 345

Catelan, M., Ferraro, F. R., & Rood, R. T. 2001, ApJ, 560, 970

Chaboyer, B. 1999, ASSL, 237, 111

Chaboyer, B., Demarque, P., & Sarajedini, A. 1996, ApJ, 459, 558

Chaboyer, B., Sarajedini, A., & Demarque, P. 1992, ApJ, 394, 515

Decressin, T., Meynet, G., Charbonnel, C., Prantzos, N., & Ekström, S. 2007, A&A, 464, 1029

D'Antona, F., Caloi, V., Montalbán, J., Ventura, P., Gratton, R. 2002, A&A, 395, 69

D'Antona, F., Stetson, P. B., Ventura, P., Milone, A. P., Piotto, G., & Caloi, V. 2009, MNRAS, 399, L151

Dinescu, D. I., Girard, T. M., & van Altena, W. F. 1999, AJ, 117, 1792

Dotter, A. 2008, ApJ, 687, 21

Dotter, A. et al. 2007, AJ, 134, 376 (Paper II)

Dotter, A. Chaboyer, B., Kostov, V., Jevermovíc, D., Baron, E., & Ferguson, J. W. 2008a, ApJS, 178, 89

Dotter, A., Kaluzny, J., & Thompson, I. B. 2009, IAUS, 258, 171

Dotter, A., Sarajedini, A. & Yang, S.-C., 2008b, AJ, 136, 1407

Dupree, A. K., Smith, G., & Strader, J. 2009, AJ, 138, 1485

Fusi Pecci, F., Ferraro, F. R., Bellazzini, M., Djorgovski, S., Piotto, G., & Buonanno, R. 1993, AJ, 105, 1145

Glatt, K., et al. 2008, AJ, 136, 1703

Gratton, R. G., Bragaglia, A., Carretta, E., Clementini, G., Desidera, S., Grundahl, F., & Lucatello, S. A&A, 408, 529

Gratton, R. G., Bragaglia, A., Clementini, G., Carretta, E., Di Fabrizio, L., Maio, M., & Taribello, E. A&A, 421, 937

Gratton, R., Sneden, C., & Carretta, E. 2004, ARA&A, 42, 385

Green, E. M. & Norris, J. E. 1990, ApJ, 353, L17

Harris, W. E. 1996, AJ, 112, 1487

Harris, W. E. et al. 1997, AJ, 114, 1030

Johnson, J. A. & Bolte, M. 1998, AJ, 115, 693

Johnson, J. A., Bolte, M., Stetson, P. B., Hesser, J. A., & Somerville, R. A. 1999, ApJ, 527, 199

Johnson, C. I., Pilachowski, C. A., Simmerer, J., & Schwenk, D. 2008, ApJ, 681, 1505

Koch, A., Côté, P., & McWilliam, A. 2009, A&A, 506, 729

Kraft, R. P. & Ivans, I. I. 2003, PASP, 115, 143 (KI03)

Lee, Y.-W. 1989, Ph.D. Thesis, Yale University, New Haven, CT.

Lee, Y.-W., 1991, ApJ, 373, 43

Lee, Y.-W., Demarque, P., & Zinn, R. J. 1990, ApJ, 350, 155

Lee, Y.-W., Demarque, P.,& Zinn, R. J. 1994, ApJ, 423, 248

Lee, Y.-W., Joo, J.-M., Sohn, Y.-J., Rey, S.-C., Lee, H.-C., & Walker, A. R. 1999, Nature, 402, 55

Mackey, A. D. & Gilmore, G. F. 2004, MNRAS, 355, 504

Mackey, A. D. & van den Bergh, S. 2005, MNRAS, 360, 631

Marín-Franch, A. et al. 2009, ApJ, 694, 1498 (Paper VII)

Marino, A. F., Villanova, S., Piotto, G., Milone, A. P., Momany, Y., Bedin, L. R., & Medling, A. M. 2008, A&A, 490, 625

McDonald, I, van Loon, J. Th., Decin, L., Boyer, M. L., Dupree, A. K., Evans, A., Gehrz, R. D., & Woodward, C. E., MNRAS, 394, 831

Mészáros, S., Avrett, E. H., Dupree, A. K., AJ, 138, 615

Milone, A. et al. 2008, ApJ, 673, 241 (Paper III)

Origlia, L. Rood, R. T., Fabbri, S., Ferraro, F. R., Fusi Pecci, F., & Rich, R. M. 2007, ApJ, 667, 850

Pietrinferni, A., Cassisi, S., Salaris, M., & Castelli, F. 2004, ApJ, 612, 168

Pietrinferni, A., Cassisi, S., Salaris, M., & Castelli, F. 2006, ApJ, 642, 797

Pietrinferni, A., Cassisi, S., Salaris, M., Percival, S. & Ferguson, J. W. 2009, ApJ, 697, 275

Piotto, G. 2009, IAUS, 258, 233

Piotto, G. et al. 2007, ApJ, 661, 53

Piotto, G. et al. 2002, A&A, 391, 945

Pritzl, P. J., Venn, K. A., & Irwin, M. 2005, AJ, 130, 2140

Recio-Blanco, A., Aparicio, A., Piotto, G., de Angeli, F., Djorgovski, S. G. 2006, A&A, 452, 875

Rey, S. C., Yoon, S.-J., Lee, Y.-W., Chaboyer, B., & Sarajedini, A. 2001, AJ, 122, 3219

Richer, H. B. et al. 1996, ApJ, 463, 602

Rood, R. T. 1973, ApJ, 184, 815

Rosenberg, A., Saviane, I., Piotto, G., & Aparicio, A. AJ, 118, 2306

Salaris, M., Chieffi, A. & Straniero, O. 1993, ApJ, 414, 580

Salaris, M., Riello, M., Cassisi, S., & Piotto, G. 2004, A&A, 420, 911

Sandage, A. R. 1953, AJ, 58, 61

Sandage, A. & Wallerstein, G. 1960, ApJ, 131, 598

Sandage, A. & Wildey, R. 1967, ApJ, 150, 469

Sandquist, E. & Hess, J. M. 2008, AJ, 136, 2259

Sarajedini, A. 1999, ASPC, 165, 295

Sarajedini, A. et al. 2007, AJ, 133, 1658 (Paper I)

Sarajedini, A. & Demarque, P. 1990, ApJ, 365, 219

Sarajedini, A. & King, C. R. 1989, AJ, 98, 1624

Sarajedini, A., Lee, Y. W., & Lee, D. H. 1995, ApJ, 450, 712

Scholz, R.-D., Odenkirchen, M., Hirte, S., Irwin, M. J., Borngen, F., & Ziener, R., 1996, MNRAS, 278, 251

Searle, L. & Zinn, R. 1978, ApJ, 225, 357

Shetrone, M. D. & Keane, M. J. 2000, AJ, 119, 840

Siegel, M. et al. 2007, ApJ, 667, 57

Sirianni, M. et al. 2005, PASP, 117, 1049

Smith, G. 2004, Observatory, 124, 365

Sneden, C., Kraft, R. P., Guhathakurta, P., Peterson, R. C., Fulbright, J. P. 2004, AJ, 127, 2162

Stetson, P. B.et al. 1999, AJ, 117, 247

Sweigart, A. V. & Catelan, M. 1998, ApJ, 501, L63

van den Bergh, S. 1965, JRASC, 59, 151

van den Bergh, S. 1967, AJ, 72, 70

VandenBerg, D. A. 2000, ApJS, 129, 315

VandenBerg, D. A., Bolte, M., & Stetson, P. B. 1990, AJ, 100, 445

VandenBerg, P. B. & Durrell, P. R. 1990, AJ, 99, 221

Ventura, P., Caloi, V., D'Antona, F., Ferguson, J., Milone, A., & Piotto, G. 2009, MNRAS, 399, 934

Zinn, R. & West, M. J. 1984, ApJS, 55, 45 (ZW84)

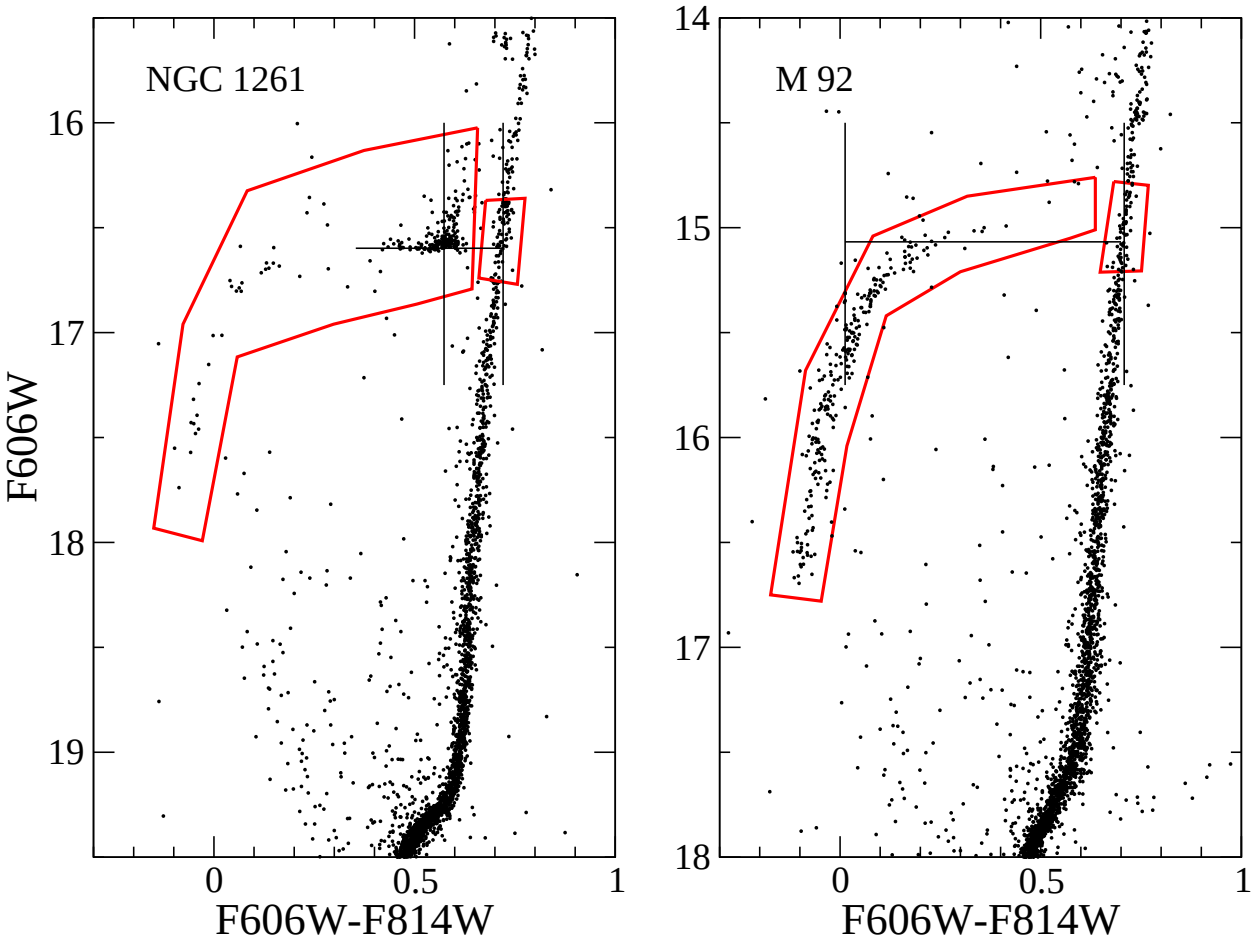

Fig. 1.— Portions of NGC 1261 and M 92 (NGC 6341) CMDs are shown. Thick lines indicate the regions that were selected to determine the median HB colors. Thin lines indicate measured quantities: vertical lines indicate the median colors of the HB and RGB; the horizontal line indicates the level of the HB.

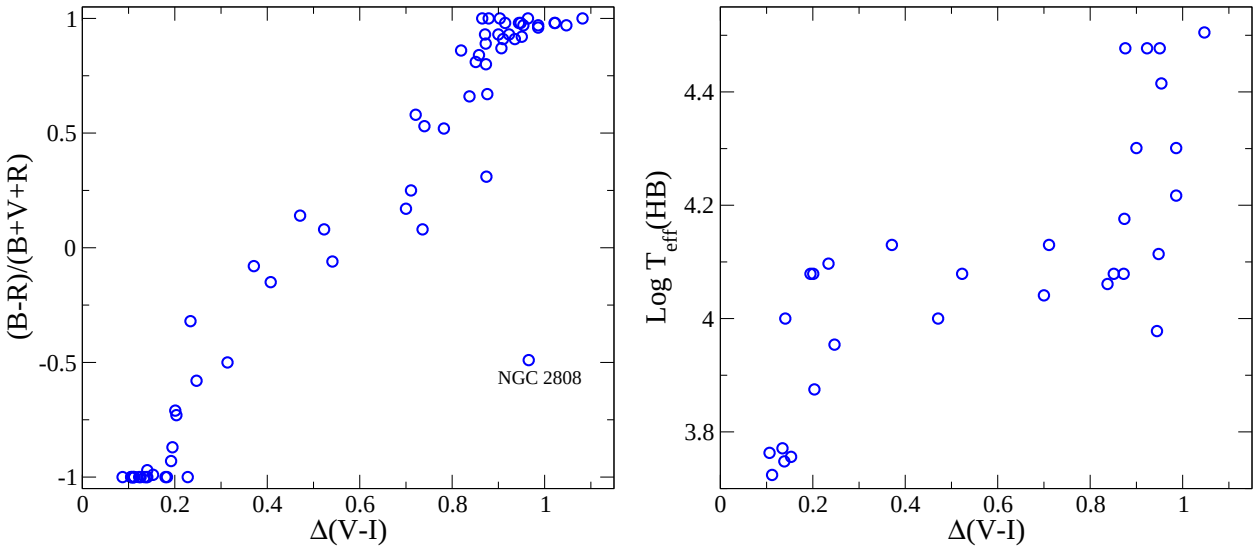

Fig. 2.— *Left:* Comparison of $\Delta(V-I)$ from this paper with (B−R)/(B+V+R) from Mackey & van den Bergh (2005) for all 66 GCs in the sample. *Right:* Comparison of $\Delta(V-I)$ and Log $T_{\rm eff}$(HB) from Recio-Blanco et al. (2006) for the 30 GCs common to both studies.

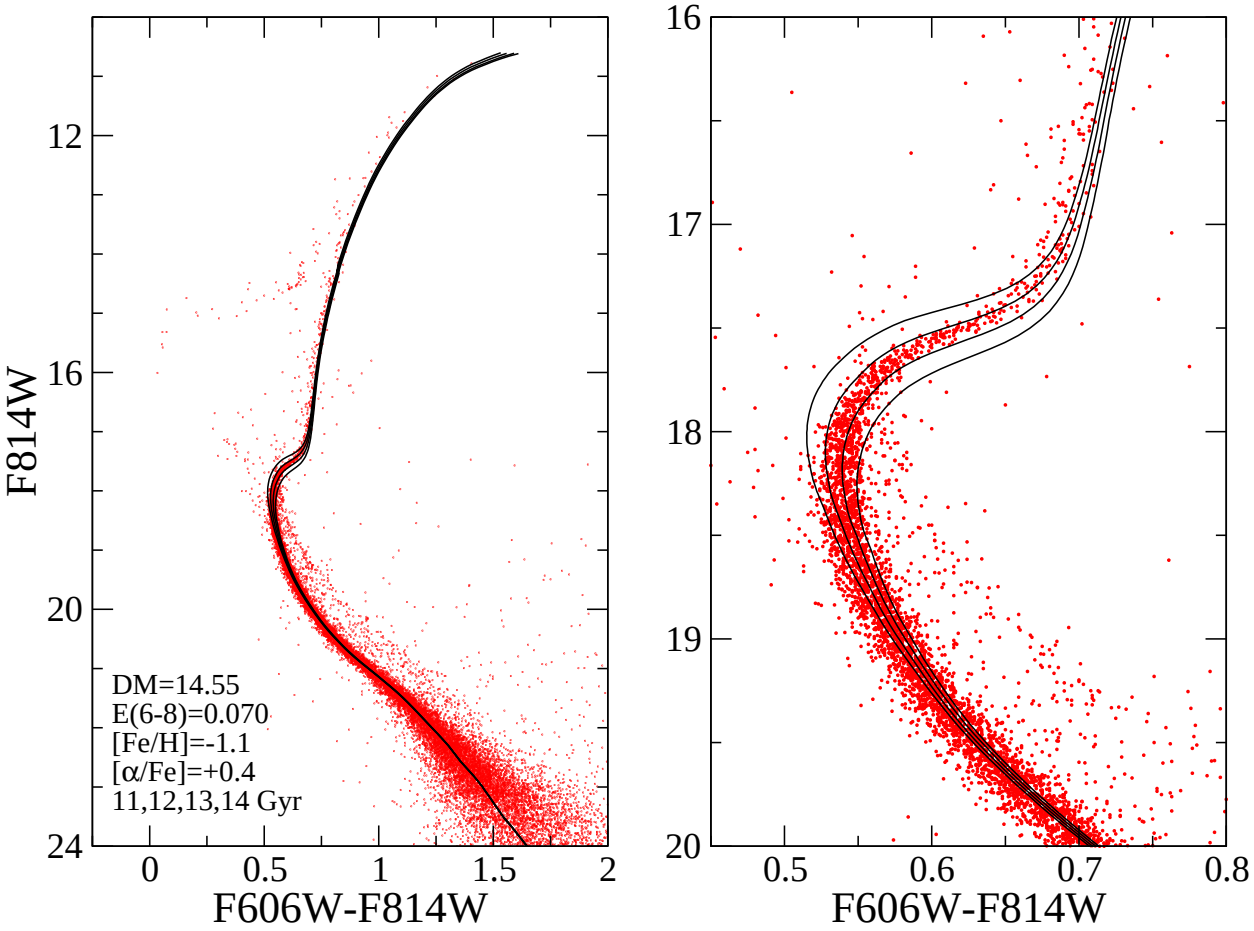

Fig. 3.— Isochrone fits to the CMD of NGC 6362; the fit parameters are listed on the figure. The left panel shows the full CMD to indicate the agreement between the models and the data on the RGB and unevolved main sequence. The right panel focuses on the main sequence turnoff region to indicate how the age was determined.

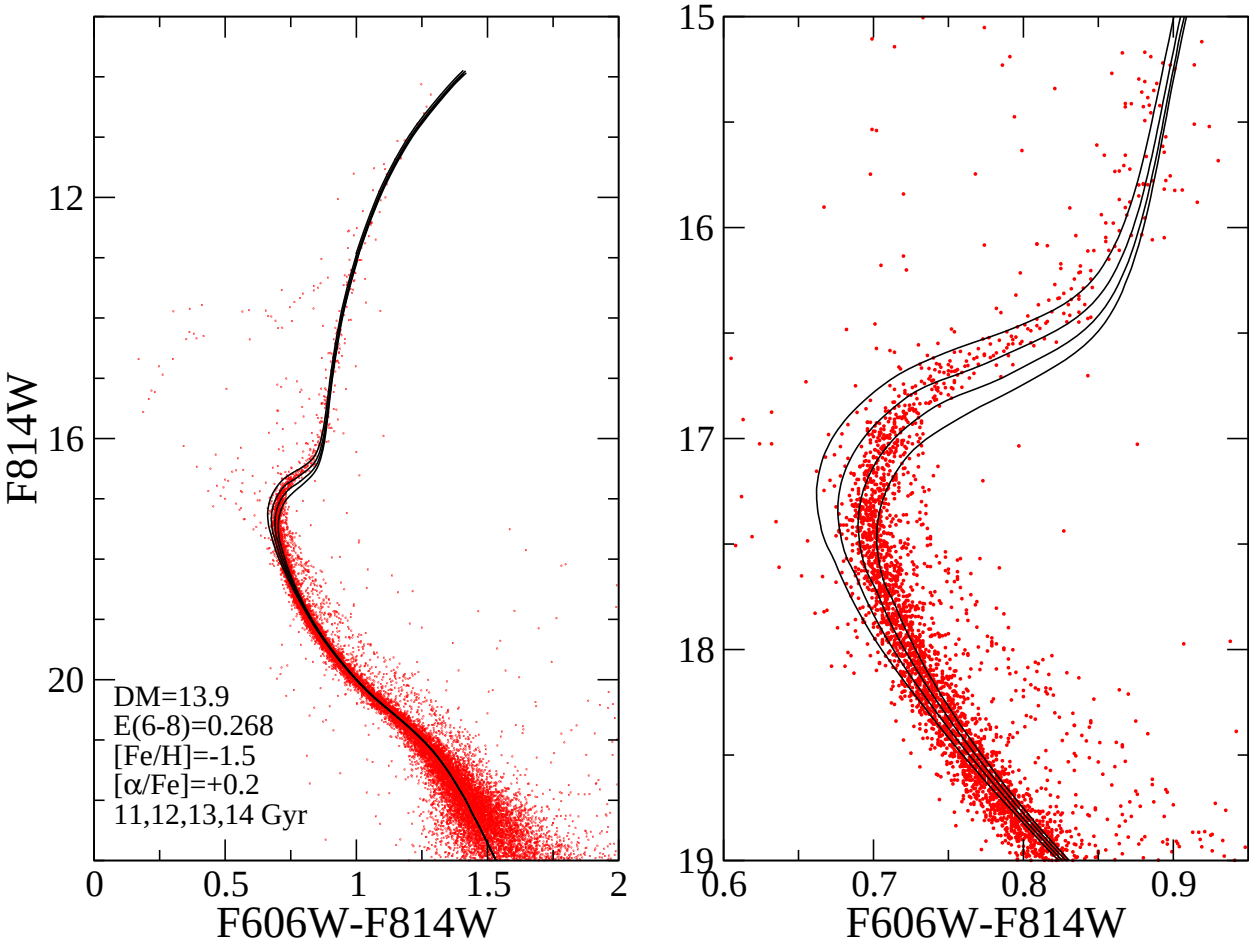

Fig. 4.— Same as Figure 3 but showing the differential reddening corrected CMD of NGC 3201.

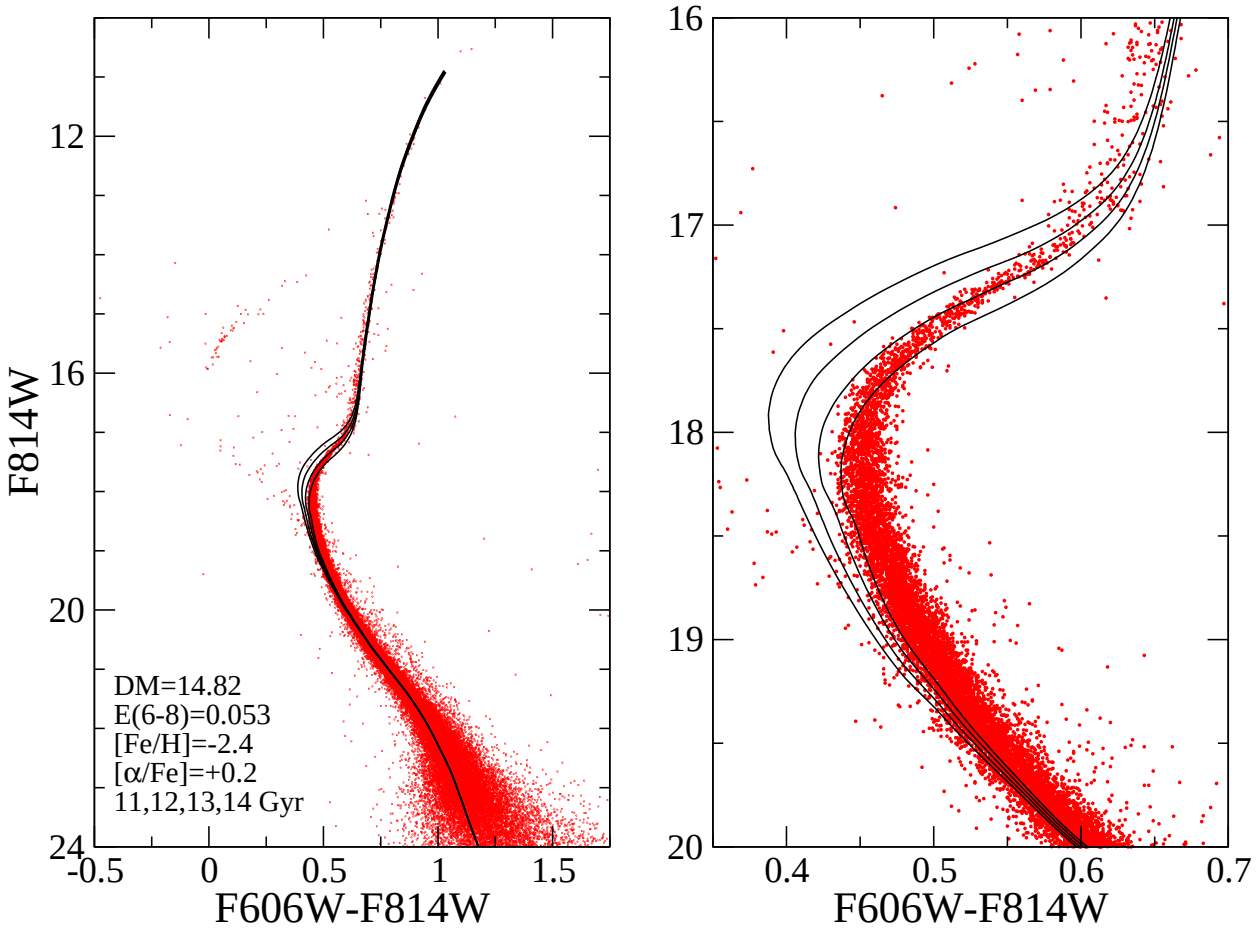

Fig. 5.— Same as Figure 3 but showing NGC 7099.

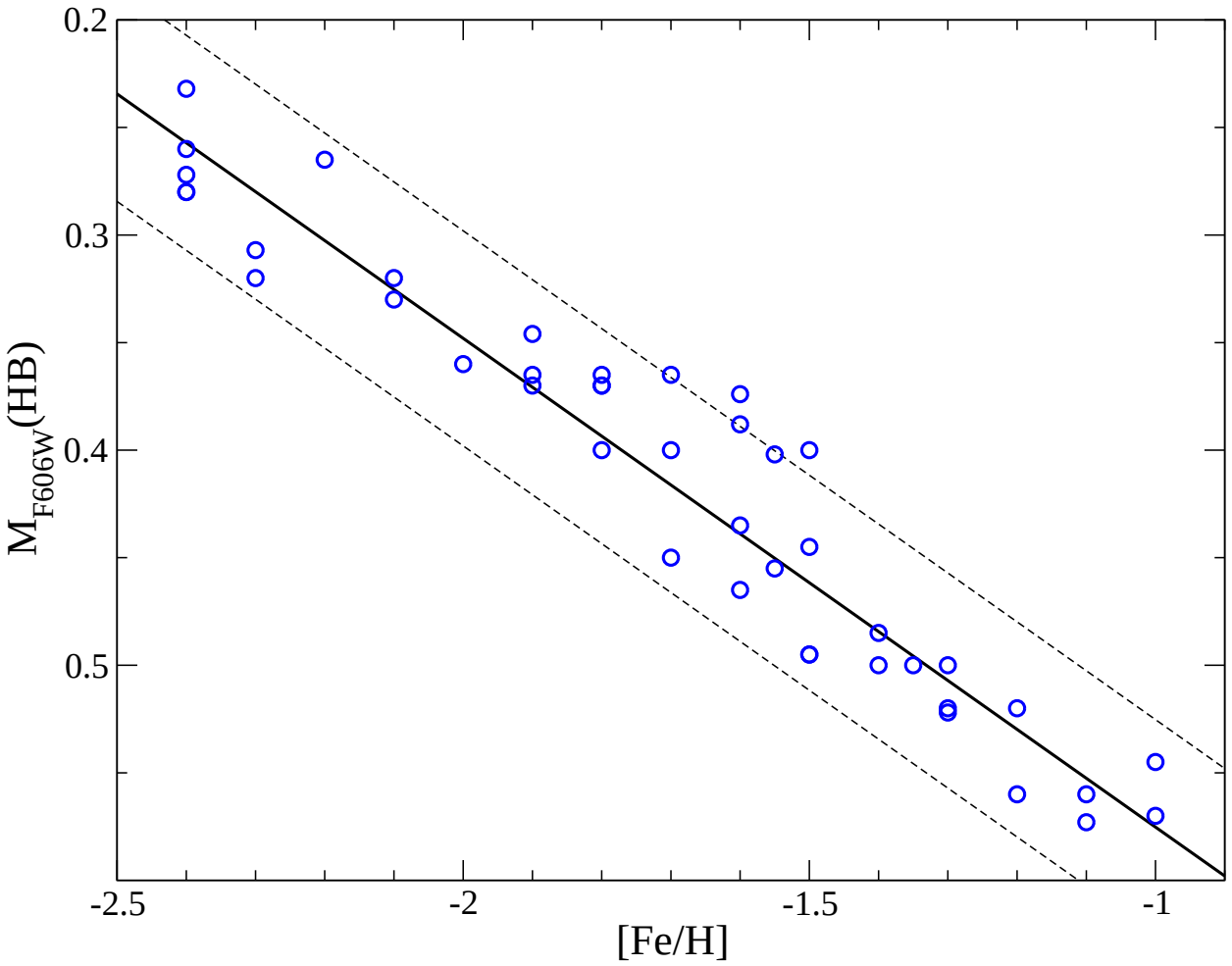

Fig. 6.— Absolute magnitude of the HB in $F606W$ as a function of metallicity. The best fit line is shown as a solid line. The dashed lines indicate ± 0.05 mag above and below the best fit line, which corresponds to the estimated uncertainty in the apparent magnitude of the HB as mentioned in §3.1.

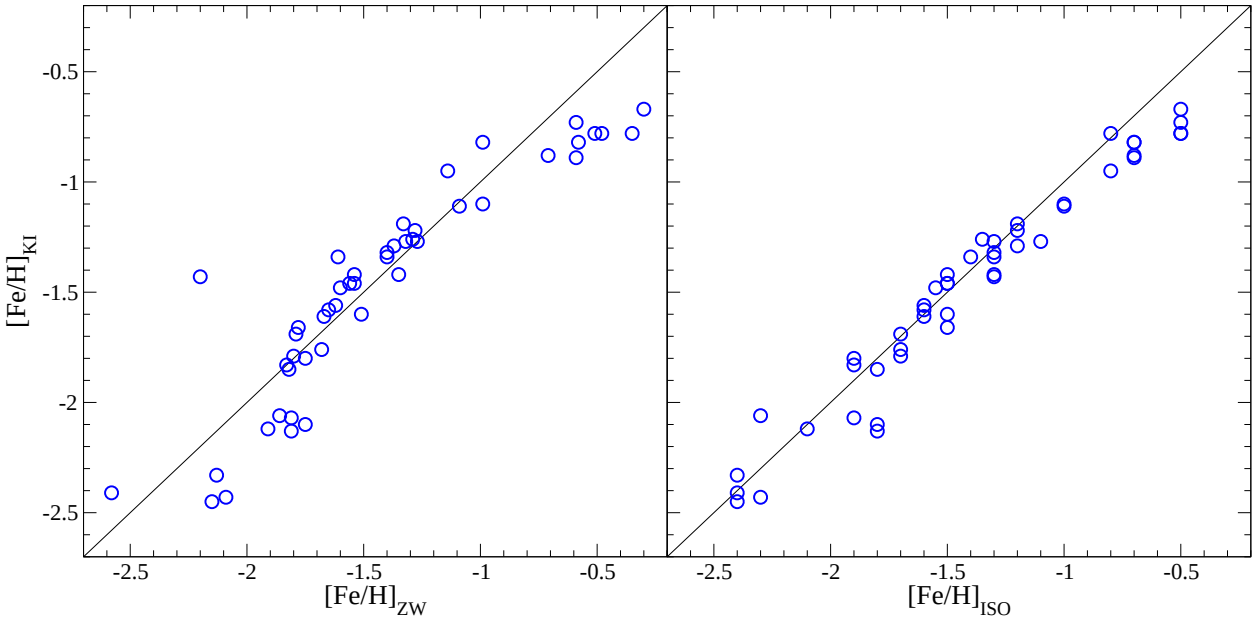

Fig. 7.— Comparison of the [Fe/H] scales from Table 2 and ZW84 with the KI03 scale for 47 GCs. The horizontal and vertical scales are the same in both panels. The solid line in each panel indicates equality.

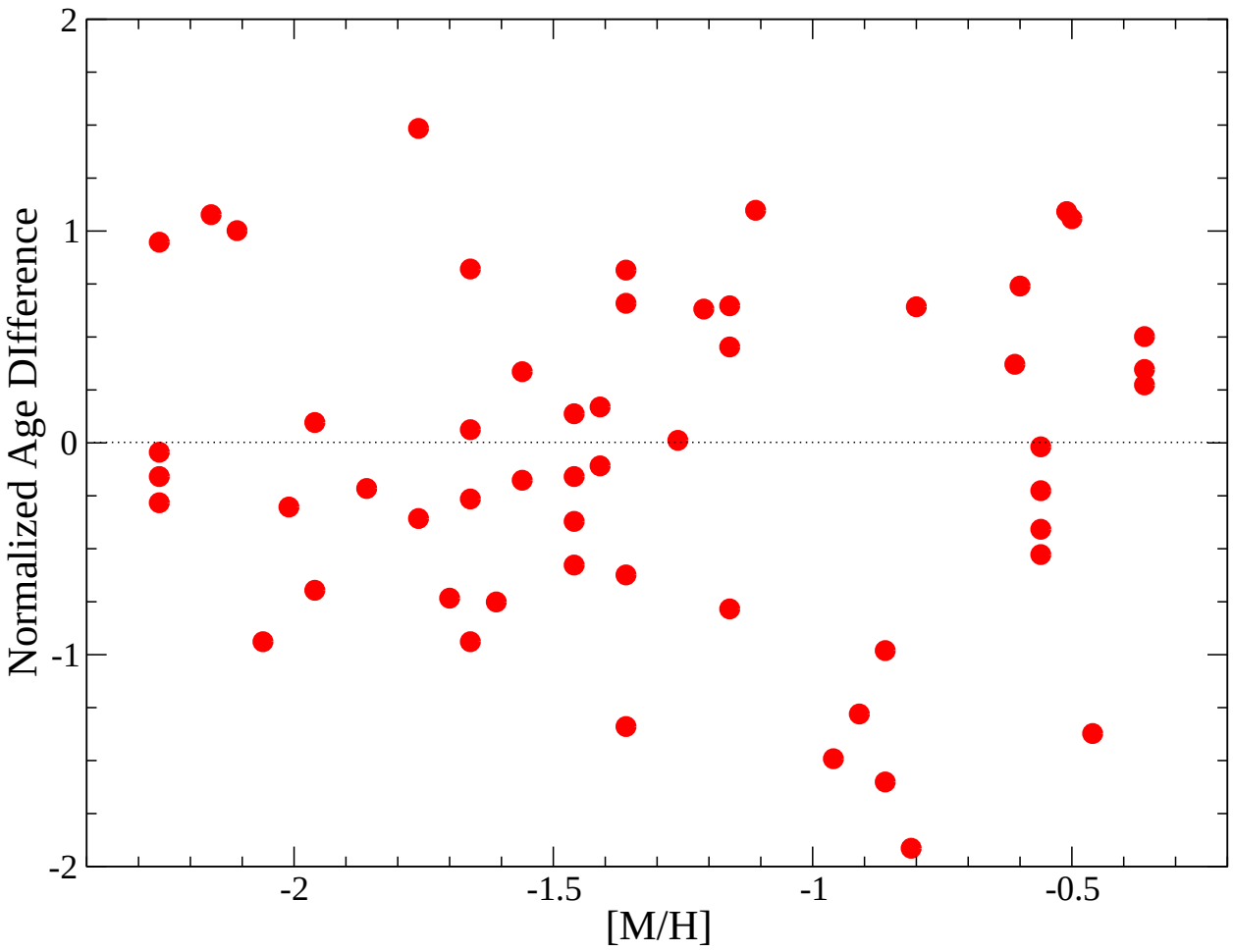

Fig. 8.— The normalized difference in age between this study and Paper VII as a function of metallicity. Age difference is presented in the sense that ΔAge = Age(ThisPaper)−Age(PaperVII) assuming, for consistency, ages from the latter based on the isochrones from Paper II and the ZW84 metallicity scale and normalized by dividing by the quadrature sum of the age uncertainties from both sources.

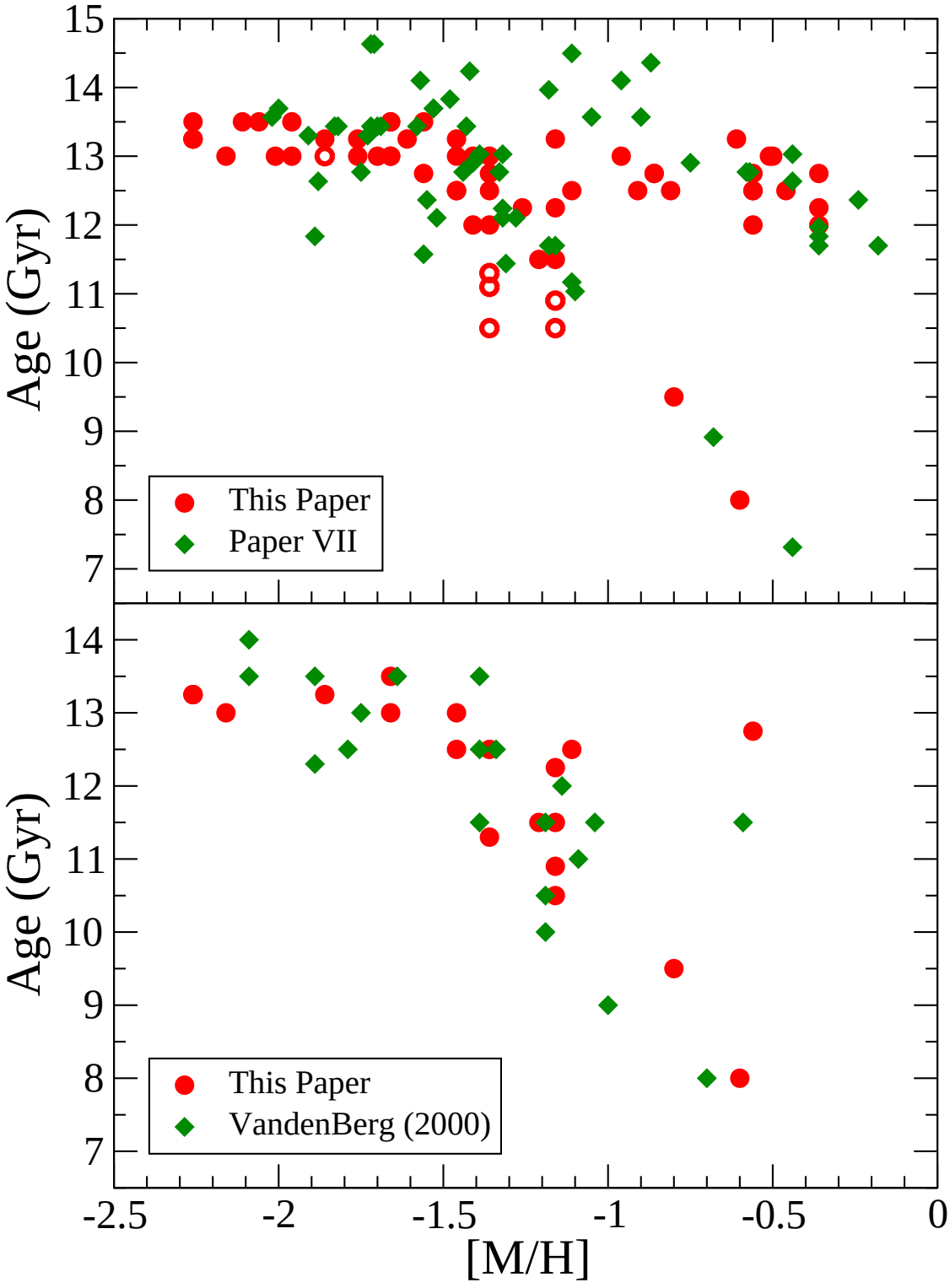

Fig. 9.— *Top:* Age-metallicity relations from the present study and Paper VII for the 55 GCs in common. The open circles are the outer halo GCs. *Bottom:* Age-metallicity relations from the present study and VandenBerg (2000) for the 20 GCs in common.

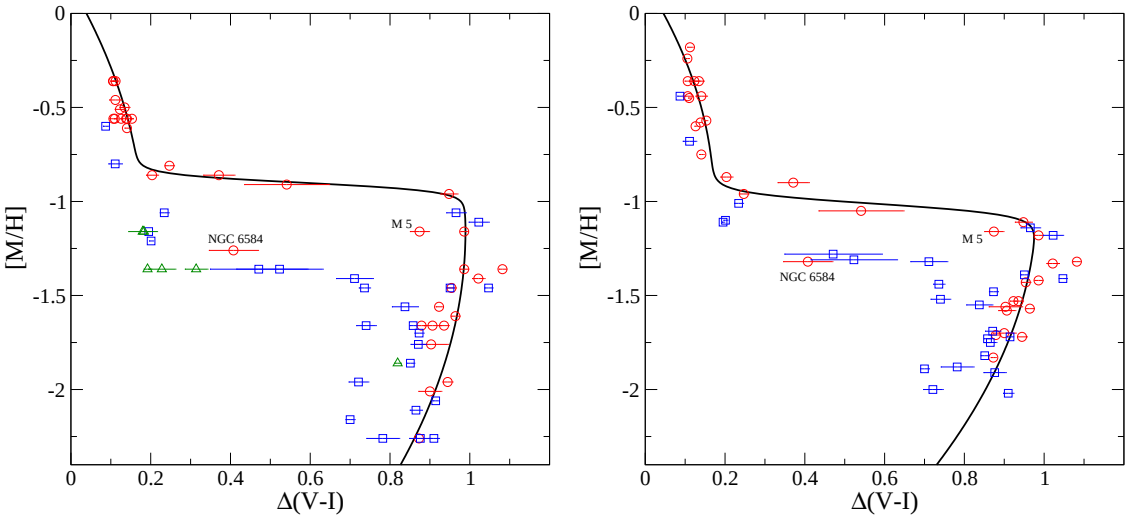

Fig. 10.— The metallicity-HB morphology diagram showing the inner (circles) and outer (squares) halo GCs from the ACS Survey. The six most distant GCs are shown as triangles. Error bars are from §3.2; fitting functions are shown as solid lines. The left panel shows the metallicity scale from Table 2; the right panels shows the ZW84 metallicity scale from Paper VII.

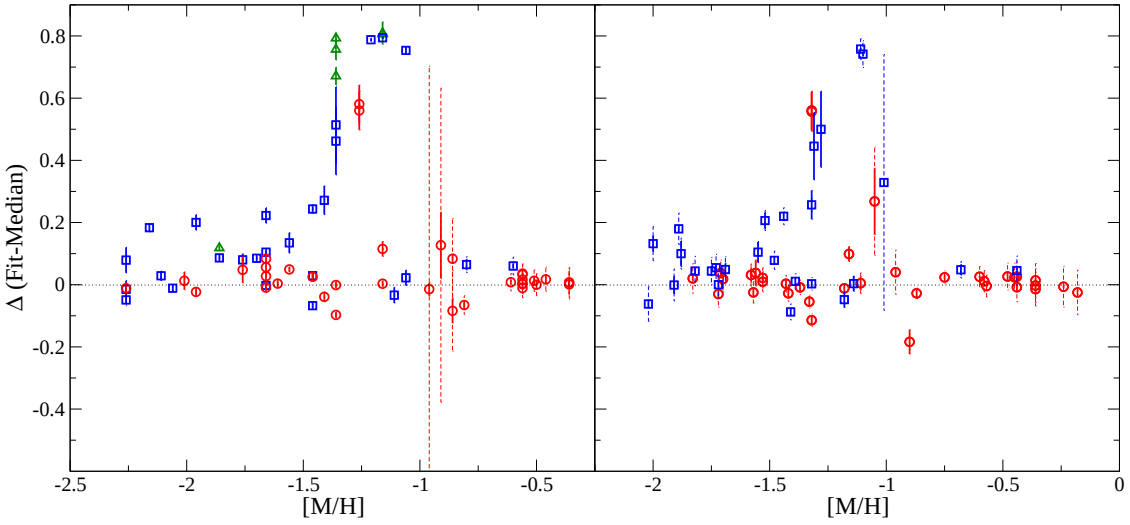

Fig. 11.— Difference between fitted and measured $\Delta(V-I)$ values as a function of [M/H]. The symbols and layout are the same as in Figure 10. The solid error bars are from measurement uncertainty in $\Delta(V-I)$ alone; the dashed error bars add the effect of metallicity uncertainty.

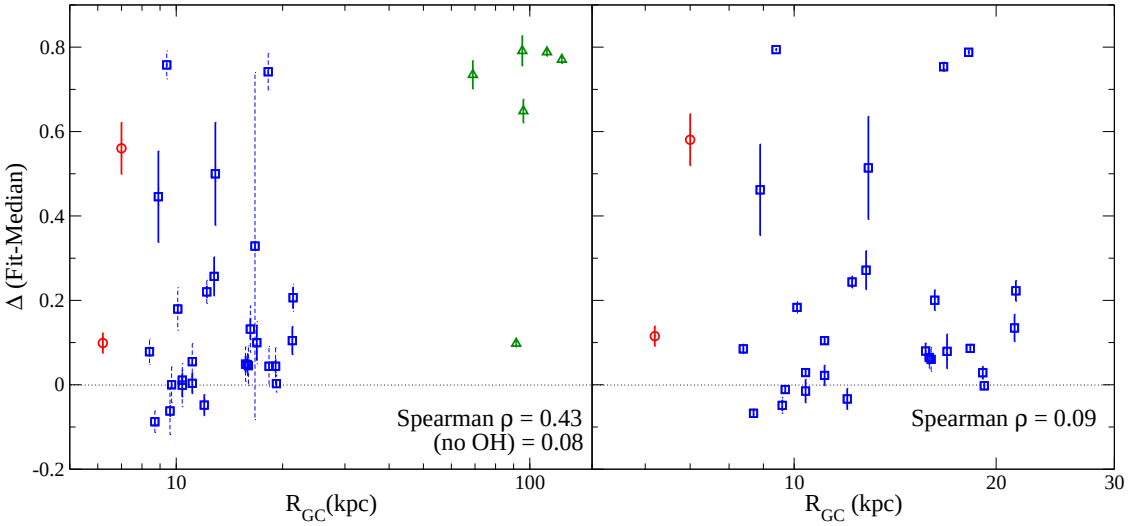

Fig. 12.— The difference between fit and measured $\Delta(V-I)$ values as a function of R_{GC}. Symbols and layout are as in Figure 11. The circles are M 5 (near the dotted line) and NGC 6584 (further away). Included on the figure is the value of the Spearman rank coefficient, see text for details. The phrase 'no OH' means that the 6 most distant GCs were omitted from the Spearman coefficient calculation.

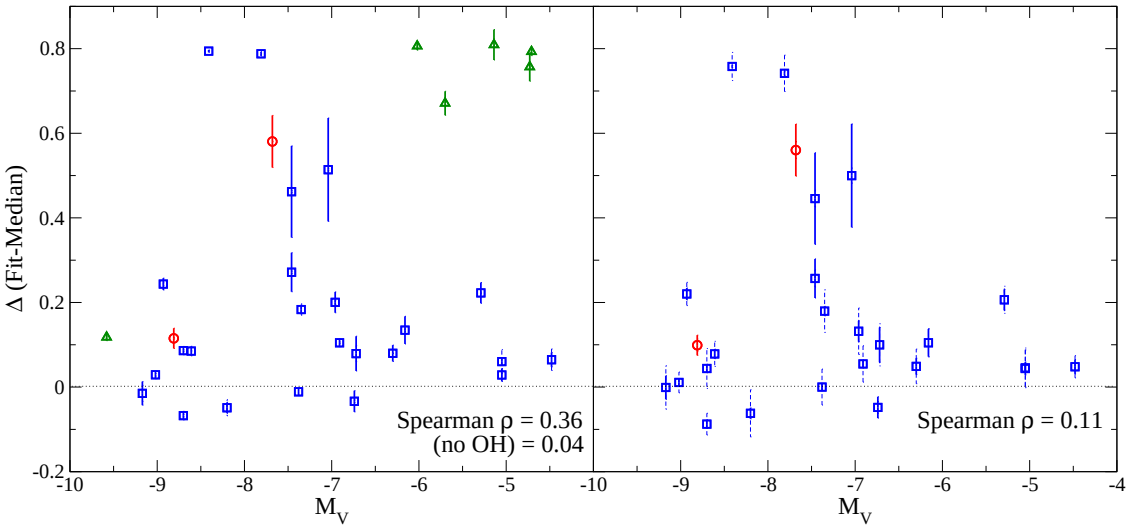

Fig. 13.— Similar to Figure 12 but as a function of M_V.

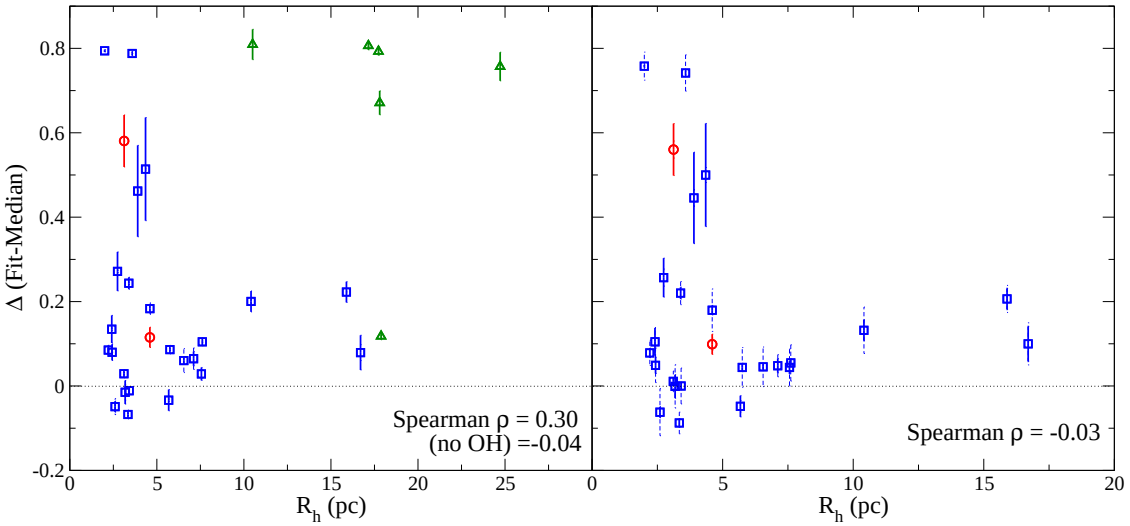

Fig. 14.— Similar to Figure 12 but as a function of R_h.

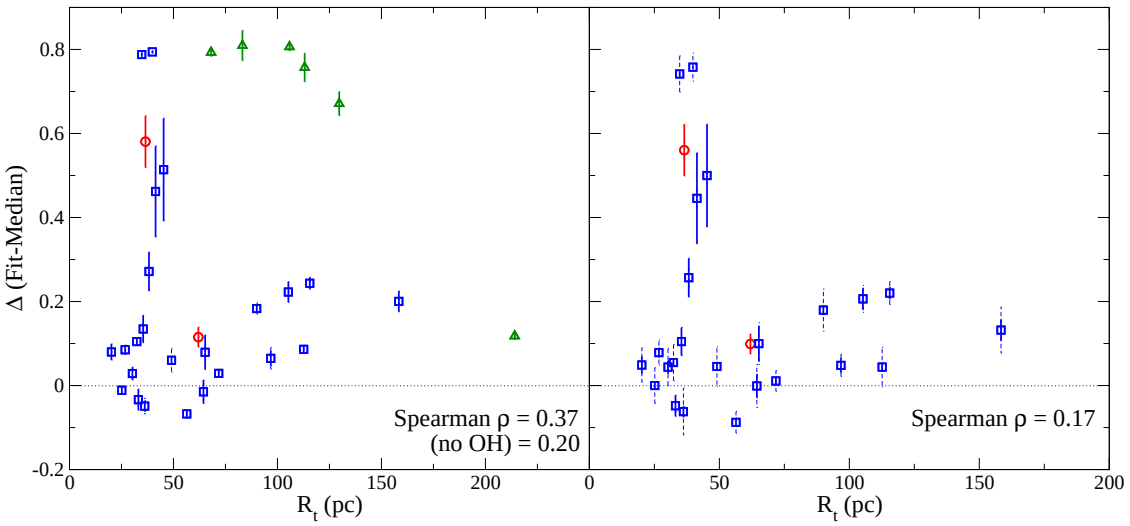

Fig. 15.— Similar to Figure 12 but as a function of R_t.

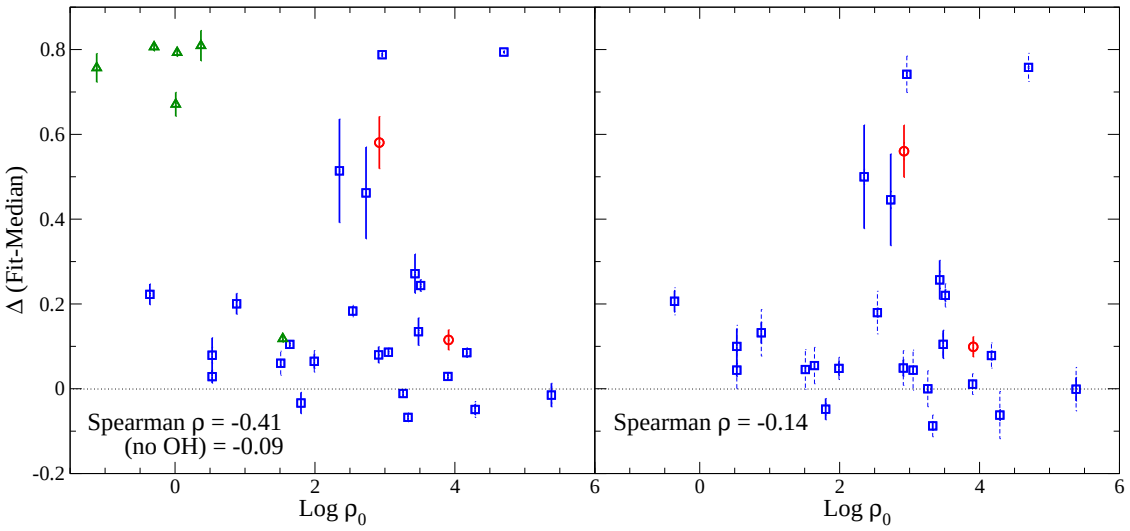

Fig. 16.— Similar to Figure 12 but as a function of Log ρ_0.

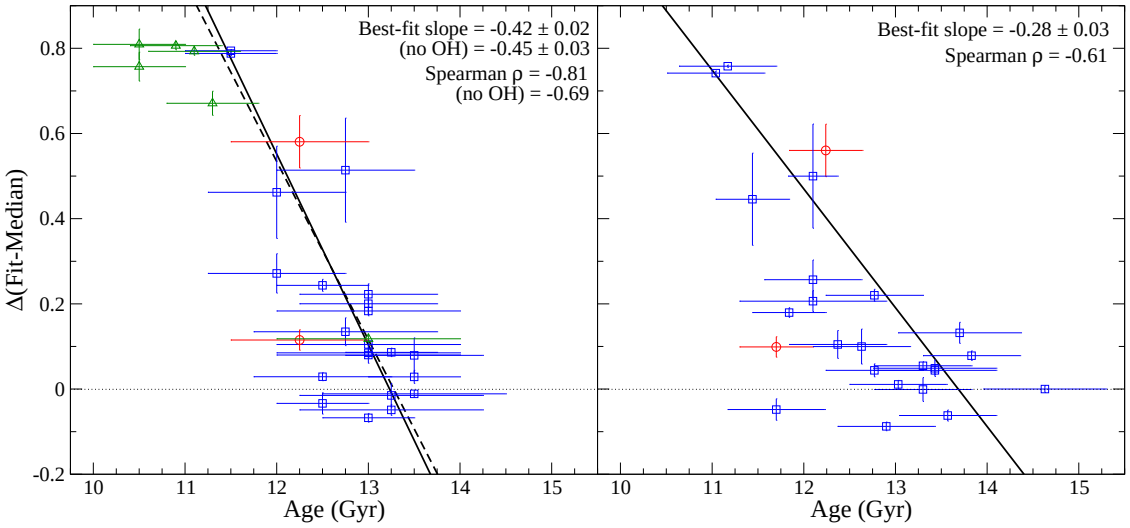

Fig. 17.— Similar to Figure 12 but as a function of age. The left panel shows the ages reported in Table 2 while the right panel shows the D07/ZW84 ages from Paper VII. The solid line is a fit to the ACS Survey data alone; the dashed line is a fit that includes the six outer halo GCs. The two youngest GCs, Pal 12 and Ter 7, have been excluded from this figure and calculation of the coefficients, see text for discussion.

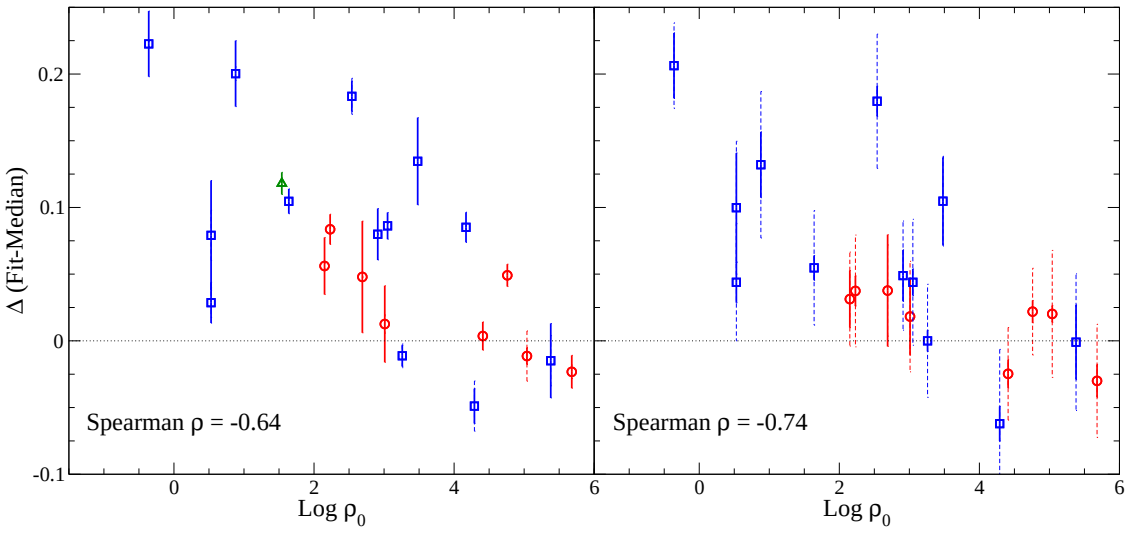

Fig. 18.— Central density (Log ρ_0) vs. Δ(Fit − Measured) showing only the metal poor GCs ([M/H] < -1.5). As with Figures 11 through 17, the left and right panels show results based on the two fitting functions determined in §5.1. Symbols are the same as in Figure 10.

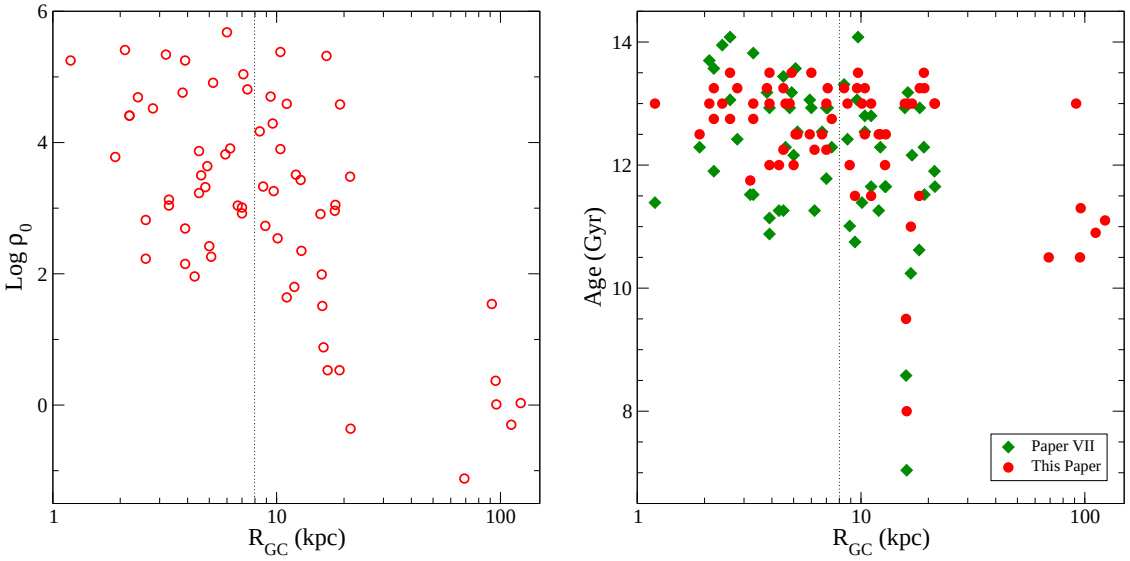

Fig. 19.— The dependence of central density (left panel) and age (right panel) on R_{GC}. The boundary assigned between the inner and outer halo is indicated by the dotted line at 8 kpc. The age plot shows results from both §4.2 (circles) and Paper VII (diamonds). R_{GC} and ρ_0 data are from the Harris catalog.

Table 1. Horizontal Branch Parameters

ID	F606W(HB)	$(V-I)_{\rm HB}$ Median	$(V-I)_{\rm HB}$ MAD	$(V-I)_{\rm RGB}$ Median	$\Delta(V-I)$
Arp 2	18.05	0.316 ± 0.017	0.200	1.056 ± 0.018	0.740 ± 0.025
Lyngå7	17.10	1.863 ± 0.003	0.034	1.974 ± 0.015	0.111 ± 0.015
NGC 104	13.90	0.916 ± 0.002	0.023	1.069 ± 0.002	0.153 ± 0.003
NGC 288	15.35	-0.018 ± 0.023	0.127	1.004 ± 0.011	1.022 ± 0.025
NGC 362	15.33	0.786 ± 0.003	0.083	0.981 ± 0.001	0.195 ± 0.003
NGC 1261	16.60	0.762 ± 0.004	0.129	0.963 ± 0.003	0.201 ± 0.005
NGC 1851	16.00	0.764 ± 0.011	0.272	0.998 ± 0.002	0.234 ± 0.011
NGC 2298	16.00	0.332 ± 0.018	0.123	1.203 ± 0.007	0.871 ± 0.019
NGC 2808	16.10	0.235 ± 0.025	0.439	1.201 ± 0.002	0.966 ± 0.025
NGC 3201	14.60	0.767 ± 0.108	0.270	1.290 ± 0.011	0.523 ± 0.108
NGC 4147	16.85	0.103 ± 0.031	0.136	0.941 ± 0.011	0.838 ± 0.033
NGC 4590	15.65	0.291 ± 0.011	0.147	0.991 ± 0.003	0.700 ± 0.011
NGC 4833	15.50	0.451 ± 0.029	0.154	1.351 ± 0.003	0.900 ± 0.029
NGC 5024	16.80	0.090 ± 0.009	0.088	0.941 ± 0.003	0.851 ± 0.010
NGC 5053	16.60	0.145 ± 0.041	0.158	0.927 ± 0.003	0.782 ± 0.041
NGC 5272	15.55	0.207 ± 0.014	0.208	0.943 ± 0.002	0.736 ± 0.014
NGC 5286	16.40	0.372 ± 0.011	0.182	1.245 ± 0.003	0.873 ± 0.011
NGC 5466	16.45	0.208 ± 0.024	0.124	0.929 ± 0.006	0.721 ± 0.025
NGC 5904	14.90	0.120 ± 0.024	0.230	0.994 ± 0.001	0.874 ± 0.024
NGC 5927	16.35	1.490 ± 0.002	0.025	1.602 ± 0.006	0.112 ± 0.007
NGC 5986	16.40	0.357 ± 0.011	0.136	1.311 ± 0.004	0.954 ± 0.012
NGC 6093	16.20	0.275 ± 0.008	0.153	1.198 ± 0.003	0.923 ± 0.008
NGC 6101	16.50	0.203 ± 0.007	0.091	1.061 ± 0.005	0.858 ± 0.009
NGC 6121	13.17	0.987 ± 0.106	0.252	1.528 ± 0.010	0.541 ± 0.106
NGC 6144	16.20	0.612 ± 0.009	0.100	1.491 ± 0.007	0.879 ± 0.011
NGC 6171	15.40	1.296 ± 0.013	0.104	1.499 ± 0.009	0.204 ± 0.015
NGC 6205	14.85	-0.091 ± 0.010	0.122	0.956 ± 0.002	1.047 ± 0.010
NGC 6218	14.60	0.227 ± 0.009	0.099	1.213 ± 0.004	0.986 ± 0.009
NGC 6254	14.80	0.269 ± 0.015	0.113	1.290 ± 0.004	1.022 ± 0.016
NGC 6304	15.95	1.556 ± 0.002	0.020	1.662 ± 0.004	0.105 ± 0.004
NGC 6341	15.05	0.036 ± 0.013	0.093	0.946 ± 0.004	0.910 ± 0.013
NGC 6352	14.95	1.249 ± 0.004	0.025	1.372 ± 0.013	0.123 ± 0.013
NGC 6362	15.18	0.817 ± 0.009	0.193	1.064 ± 0.007	0.247 ± 0.012
NGC 6366	15.25	1.817 ± 0.010	0.030	1.957 ± 0.011	0.141 ± 0.014
NGC 6388	17.00	1.344 ± 0.002	0.172	1.470 ± 0.002	0.126 ± 0.003
NGC 6397	12.90	0.217 ± 0.007	0.066	1.162 ± 0.010	0.944 ± 0.012

Table 1—Continued

ID	F606W(HB)	$(V-I)_{\rm HB}$ Median	$(V-I)_{\rm HB}$ MAD	$(V-I)_{\rm RGB}$ Median	$\Delta(V-I)$
NGC 6441	17.65	1.501 ± 0.002	0.154	1.611 ± 0.002	0.110 ± 0.003
NGC 6496	16.20	1.224 ± 0.004	0.023	1.331 ± 0.007	0.107 ± 0.008
NGC 6535	15.65	0.554 ± 0.041	0.127	1.457 ± 0.011	0.903 ± 0.042
NGC 6541	15.15	0.112 ± 0.010	0.107	1.076 ± 0.004	0.964 ± 0.011
NGC 6584	16.40	0.640 ± 0.061	0.215	1.048 ± 0.003	0.408 ± 0.062
NGC 6624	15.85	1.248 ± 0.003	0.025	1.383 ± 0.012	0.135 ± 0.012
NGC 6637	15.75	1.092 ± 0.002	0.020	1.230 ± 0.002	0.138 ± 0.003
NGC 6652	15.77	1.030 ± 0.004	0.021	1.171 ± 0.004	0.141 ± 0.006
NGC 6656	14.15	0.438 ± 0.011	0.141	1.373 ± 0.004	0.935 ± 0.012
NGC 6681	15.63	0.074 ± 0.010	0.112	1.060 ± 0.002	0.986 ± 0.010
NGC 6717	15.53	0.268 ± 0.021	0.128	1.216 ± 0.003	0.948 ± 0.021
NGC 6723	15.30	0.704 ± 0.039	0.301	1.075 ± 0.003	0.371 ± 0.039
NGC 6752	13.70	-0.058 ± 0.009	0.102	1.024 ± 0.003	1.082 ± 0.010
NGC 6779	16.15	0.305 ± 0.007	0.110	1.220 ± 0.003	0.914 ± 0.008
NGC 6809	14.35	0.154 ± 0.021	0.097	1.060 ± 0.004	0.906 ± 0.021
NGC 6838	14.21	1.185 ± 0.009	0.021	1.291 ± 0.005	0.106 ± 0.010
NGC 6934	16.78	0.355 ± 0.046	0.251	1.066 ± 0.005	0.711 ± 0.046
NGC 6981	16.73	0.537 ± 0.122	0.247	1.008 ± 0.007	0.471 ± 0.122
NGC 7078	15.75	0.131 ± 0.028	0.196	1.007 ± 0.002	0.876 ± 0.028
NGC 7089	15.95	0.043 ± 0.009	0.148	0.993 ± 0.002	0.951 ± 0.009
NGC 7099	15.12	0.087 ± 0.005	0.077	0.960 ± 0.004	0.872 ± 0.006
Pal 12	16.90	0.908 ± 0.005	0.008	1.019 ± 0.016	0.111 ± 0.017
Terzan 7	17.67	1.028 ± 0.004	0.012	1.115 ± 0.005	0.087 ± 0.007
Terzan 8	17.90	0.230 ± 0.011	0.111	1.095 ± 0.011	0.865 ± 0.015
Additional GCs					
AM-1	20.92	0.799 ± 0.008	0.021	0.991 ± 0.005	0.192 ± 0.009
Eridanus	20.23	0.829 ± 0.015	0.017	1.009 ± 0.033	0.180 ± 0.036
NGC 2419	20.35	0.198 ± 0.008	0.155	1.017 ± 0.002	0.819 ± 0.008
Pal 3	20.40	0.688 ± 0.021	0.087	1.002 ± 0.019	0.314 ± 0.028
Pal 4	20.65	0.816 ± 0.008	0.018	0.999 ± 0.006	0.183 ± 0.010
Pal 14	20.00	0.828 ± 0.021	0.035	1.056 ± 0.027	0.228 ± 0.034

Note. — MAD = Mean Absolute Deviation

Table 2. Results from Isochrone Fitting

Name	[Fe/H]	[α/Fe]	DM_{F814W}	E(6−8)	Age (Gyr)
Arp 2	-1.80	0.2	17.55	0.113	13.00 ± 0.75
Lyngå7	-0.60	0.2	15.80	0.713	12.50 ± 1.00
NGC 104	-0.70	0.2	13.30	0.023	12.75 ± 0.50
NGC 288	-1.40	0.4	14.85	0.013	12.50 ± 0.50
NGC 362	-1.30	0.2	14.80	0.023	11.50 ± 0.50
NGC 1261	-1.35	0.2	16.10	0.013	11.50 ± 0.50
NGC 2298*	-1.90	0.2	15.43	0.237	13.00 ± 1.00
NGC 3201*	-1.50	0.2	13.90	0.268	12.00 ± 0.75
NGC 4147	-1.70	0.2	16.48	0.018	12.75 ± 0.75
NGC 4590	-2.30	0.2	15.30	0.056	13.00 ± 1.00
NGC 4833*	-2.30	0.4	14.84	0.353	13.00 ± 1.25
NGC 5024	-2.00	0.2	16.43	0.023	13.25 ± 0.50
NGC 5053	-2.40	0.2	16.32	0.021	13.50 ± 0.75
NGC 5272	-1.60	0.2	15.08	0.018	12.50 ± 0.50
NGC 5286*	-1.70	0.0	15.75	0.263	13.00 ± 1.00
NGC 5466	-2.10	0.2	16.12	0.023	13.00 ± 0.75
NGC 5904	-1.30	0.2	14.38	0.033	12.25 ± 0.75
NGC 5927*	-0.50	0.2	15.30	0.393	12.25 ± 0.75
NGC 5986*	-1.60	0.2	15.73	0.295	13.25 ± 1.00
NGC 6093*	-1.70	0.2	15.55	0.213	13.50 ± 1.00
NGC 6101	-1.80	0.2	16.03	0.113	13.00 ± 1.00
NGC 6121*	-1.20	0.4	12.20	0.423	12.50 ± 0.50
NGC 6144*	-1.80	0.2	15.40	0.448	13.50 ± 1.00
NGC 6171*	-1.00	0.2	14.45	0.418	12.75 ± 0.75
NGC 6205	-1.60	0.2	14.47	0.019	13.00 ± 0.50
NGC 6218	-1.30	0.2	13.90	0.191	13.25 ± 0.75
NGC 6254*	-1.55	0.2	14.15	0.261	13.00 ± 1.25
NGC 6304*	-0.50	0.2	14.87	0.473	12.75 ± 0.75
NGC 6341	-2.40	0.2	14.80	0.031	13.25 ± 1.00
NGC 6352*	-0.80	0.4	14.10	0.253	13.00 ± 0.50
NGC 6362	-1.10	0.4	14.55	0.070	12.50 ± 0.50
NGC 6366	-0.70	0.2	14.00	0.718	12.00 ± 0.75
NGC 6397	-2.10	0.2	12.40	0.183	13.50 ± 0.50
NGC 6496	-0.50	0.2	15.35	0.213	12.00 ± 0.75
NGC 6535	-1.90	0.2	14.85	0.443	13.25 ± 1.00
NGC 6541*	-1.90	0.4	14.68	0.118	13.25 ± 1.00
NGC 6584	-1.40	0.2	15.85	0.078	12.25 ± 0.75

Table 2—Continued

Name	[Fe/H]	[α/Fe]	DM_{F814W}	E(6−8)	Age (Gyr)
NGC 6624*	-0.50	0.0	15.05	0.253	13.00 ± 0.75
NGC 6637*	-0.70	0.2	15.05	0.163	12.50 ± 0.75
NGC 6652	-0.75	0.2	15.05	0.113	13.25 ± 0.50
NGC 6681	-1.50	0.2	15.05	0.098	13.00 ± 0.75
NGC 6717*	-1.10	0.2	14.78	0.203	13.00 ± 0.75
NGC 6723	-1.00	0.2	14.67	0.073	12.75 ± 0.50
NGC 6752	-1.50	0.2	13.26	0.053	12.50 ± 0.75
NGC 6779*	-2.20	0.2	15.65	0.248	13.50 ± 1.00
NGC 6809	-1.80	0.2	13.88	0.113	13.50 ± 1.00
NGC 6838*	-0.70	0.2	13.40	0.223	12.50 ± 0.75
NGC 6934	-1.55	0.2	16.23	0.108	12.00 ± 0.75
NGC 6981	-1.50	0.2	16.20	0.048	12.75 ± 0.75
NGC 7078	-2.40	0.2	15.40	0.083	13.25 ± 1.00
NGC 7089	-1.60	0.2	15.48	0.048	12.50 ± 0.75
NGC 7099	-2.40	0.2	14.82	0.053	13.25 ± 1.00
Pal 12	-0.80	0.0	16.40	0.033	9.50 ± 0.75
Terzan 7	-0.60	0.0	17.15	0.073	8.00 ± 0.75
Terzan 8	-2.40	0.4	17.50	0.133	13.50 ± 0.50
Additional GCs [DM_V and E($V-I$)]					
AM-1	-1.50	0.2	20.41	0.020	11.10 ± 0.50
Eridanus	-1.30	0.2	19.78	0.060	10.50 ± 0.50
NGC 2419	-2.00	0.2	20.05	0.062	13.00 ± 1.00
Pal 3	-1.50	0.2	19.89	0.060	11.30 ± 0.50
Pal 4	-1.30	0.2	20.14	0.055	10.90 ± 0.50
Pal 14	-1.50	0.2	19.51	0.045	10.50 ± 0.50

Note. — An asterisk (*) after the name indicates that the differential reddening corrected CMD was used in the isochrone analysis. $E(6-8) = E(F606W - F814W)$.

Table 3. Fitting Function Coefficients

Name	This Paper	Paper VII
a_0	0.947 ± 0.016	0.946 ± 0.015
a_1	0.809 ± 0.017	0.809 ± 0.017
a_2	0.900 ± 0.021	1.012 ± 0.036
a_3	0.022 ± 0.011	0.029 ± 0.019
b_0	-0.098 ± 0.023	-0.091 ± 0.020
b_1	-0.244 ± 0.050	-0.253 ± 0.051
b_2	-0.105 ± 0.020	-0.127 ± 0.025